to be improved with long "photon" lifetimes in the etalon and large number of photon counts making position measurements, i.e. making a device with large reflectivity r_2, and large base height, h_0. Nevertheless, the calculations have assumed the thin plate approximation, and a realistic spiral phase plate etalon starts to deviate from these approximations at around a reflectivity of $r_2 = 0.7$ as shown in chapter II, for parameters reported in this chapter and a base height of $h_0 = 0.6$cm.

The computer generated optical intensity profile comprise of many photon counts consisting of a coherent superposition of optical vortices in different orbital angular momentum states (as shown in Chapter II), and hence are strictly classical beams. This makes the spiral phase plate etalon unique in that there is an angular modulation amplitude as a function of angle which can be seen at the same time and in real time and space on the CCD detector screen. Another unique feature of the spiral phase plate etalon is that as the laser frequency is varied, the angular interference pattern rotates, repeating itself at select laser frequencies in a 2π radian angle. These are just a few examples of the unique features of a spiral phase plate etalon compared to the conventional Fabry-Perot etalon.

Additionally, the analysis undertaken in this chapter assumes that the CCD camera is shot noise limited and there are no other sources of noise in the data. In the actual experiment, other sources of noise or errors in the data can significantly decrease the sensitivity of the spiral phase plate etalon when taken into account. They include noise in the amplitude and phase of the laser intensity, errors associated with distortions of the optical intensity profile and finding its center, the other sources of noise on the CCD detector such as read noise, electronic noise...etc. The error bar on the fit parameters is expected to capture these sources of noise. Furthermore, the analytical tools developed in this chapter is computationally time efficient (i.e. Mathematica program takes less than 2 minutes to analyze a set of four images, each partitioned into hundreds of angular wedges), and relatively straightforward to use.

It will be employed to analyze the optical intensity profiles in the proceeding chapters.

CHAPTER IV

Measurement of multiple beam interference in a spiral phase plate etalon

4.1   Introduction

This chapter reports on the experimental observation and measurement of multiple beam interference in a spiral phase plate etalon. The components of the experimental apparatus is described. In addition, the experimental parameters with corresponding statistical uncertainty used to describe the spiral phase plate etalon is quantified by a weighted fit of the experimental data, and compared with theory and a computer model of the experiment based on shot noise limited assumptions. Noise sources in the experiment such as shot noise, read noise and dark noise are discussed. Systematic errors which results from improperly determining the center of the optical beam profile is also estimated from the simulations, in which the dominant source of noise is shot noise. Many of the analytic tools and precautions developed in chapter III are employed in quantifying the data. Furthermore, some of the theory developed in chapter III is reproduced in this chapter as it relates to the experiment.

4.2 Experiment

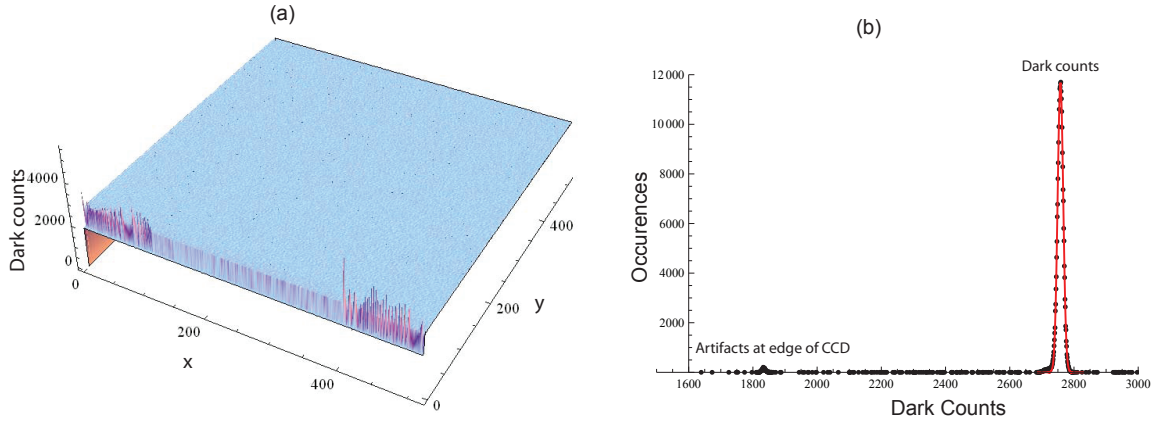### 4.2.1 CCD camera description

Figure 4.1: Dark counts on CCD camera. (a) 3D image of CCD showing presence of artifact for an exposure time of 1ms at last row of CCD for a digitization read-out rate of 5MHz. (b) Histogram of dark counts. Small histogram peak is due to artifacts at the last row of CCD and large peak is from dark count fluctuation on CCD. Both peaks fits well to a Gaussian function.

The charge coupled device (CCD) camera is an Acton photon max camera from Princeton instruments (79). There are 512 by 512 pixels on the CCD with a pixel size of $16\mu m$ by $16\mu m$, and peak counts of 65000 on each pixel. The digitization readout rate can be set to 10MHz, 5MHz, or 1MHz. For the experimental images, the data have mostly been read out at either 5MHz (See fig. 4.1) or 1MHz (See fig. 4.2) for low noise levels. There is a difference in the dark counts offset depending on whether the data is read out at 5MHz (See fig. 4.1(b)) or 1MHz (See fig. 4.2(c)).

One of the sources of noise in the CCD camera is from build-up of charge on the CCD chip over time. This charge is called dark charge and it results in noise called dark noise. The CCD background will appear less uniform with longer exposure time and warmer camera due to the presence of dark charge on the CCD. This can cause loss of dynamic range (i.e. maximum light intensity that CCD can measure)
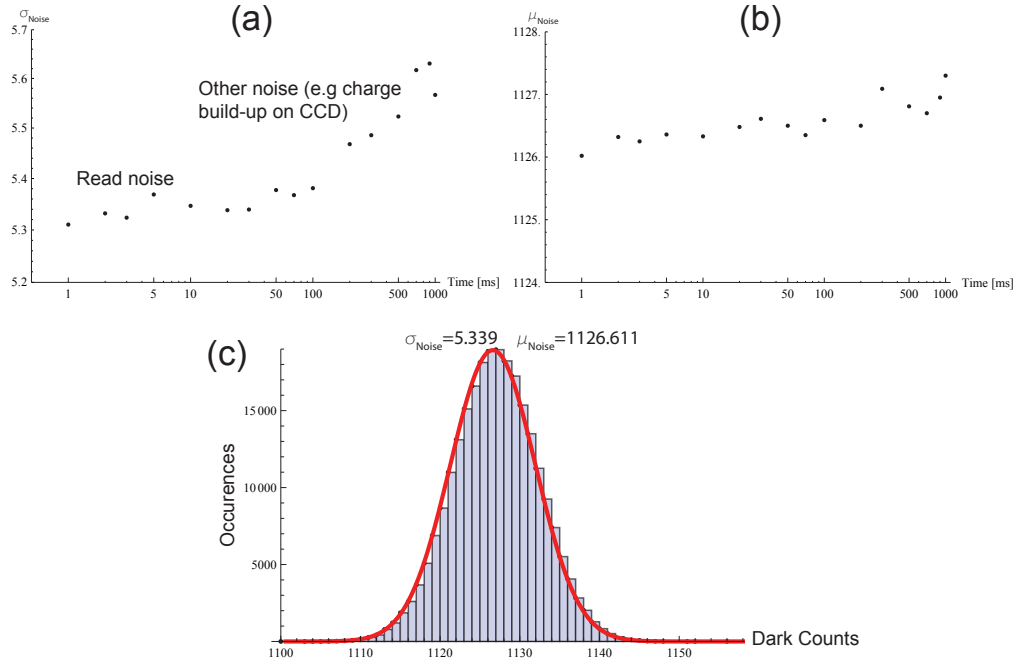
60

Figure 4.2: (a) Measured standard deviation of CCD dark count noise for different exposure times with a digitization read-out rate of 1MHz. The zero slope data points are probably from read noise, and the non-zero slope data points are probably from charge build-up on the CCD. (b) Measured mean of CCD dark count noise for different exposure times. (c) A single shot noise measurement for an exposure time of 30ms. The standard deviation is $\sigma_{Noise} = 5.33$ counts and mean is $\mu_{Noise} = 1126.61$ counts. Red curve is a fit to the data.

in the CCD. For data collection, the charge accumulated on the CCD can be cleared at specific times during which a sequence of images are taken. Nevertheless, if the accumulation time of the CCD is long, residual "dark charge" builds up on the CCD before the clearing options take effect (See fig. 4.2). The CCD dark noise is measured with the CCD screen covered to prevent ambient room light and a histogram of the "dark" counts is fitted to a Gaussian function [See fig. 4.2(c)]. The 1 standard deviation (1 std. dev.) Gaussian width of the histogram is a measure of the dark noise fluctuation on the CCD. There appears to be additional sources of noise (e.g dark noise, electronic noise etc) on the CCD chip for exposure times over 100ms regardless of CCD charge clearing option [See fig. 4.2(a)]. A dependence of the noise on exposure

time is represented in fig. 4.2. As seen in Fig. 4.2(c), there is a built-in offset in the CCD camera counts of approximately 1126.61 counts with a spread about the mean of approximately $\sigma_{Noise} = 5.33$. Hence the shot noise limit of a single frame of the CCD cannot be determined from the dark counts alone using standard methods such as making sure that the ratio of the 1 std. dev. width of the histogram is the same as the square-root of the mean. For the CCD to be shot noise limited, the mean dark counts will have to be around $\mu_{Noise} = 26$ counts since the measured standard deviation is $\sigma_{Noise} = 5.33$, to give $\frac{\sigma_{Noise}}{\sqrt{\mu_{Noise}}} \approx 1$. When analyzing the experimental data, each image is cropped by 5 to 10 pixels from the edges as there appears to be additional artifacts at the last row of pixels that read out the data from the CCD [See fig. 4.1].

Similar analysis to the one in Fig 4.2 can be used to examine the random photon count fluctuation in the background counts (not dark counts) on the CCD detector as a result of ambient room lights during the experiment. A typical background count histogram is in Fig. 4.3 with a mean of 1239.83 counts and histogram 1 std. dev. width of 6.48 counts. The background counts is approximately 1.54 std. dev. from the dark count level in Fig 4.2, indicating very low background count level. A change in noise standard deviation, σ_{Noise}, about the mean, μ_{Noise}, is expected if there are changes in shot to shot measurements in the background counts. During the pixel by pixel analysis of the data, a background subtraction is performed. The purpose of the above analysis is to ensure that the background counts is minimal and does not adversely affect the measurement of the optical angular interference pattern.

4.2.2 Spiral phase plate etalon parameters and imaging set-up

Optical transmission through a spiral phase plate etalon is probed using a well-collimated Gaussian laser beam coming out of a single mode fiber with wavelength $\lambda = 555.8410 \pm 0.0001$ nm and a $1/e^2$ beam radius of $\omega_0 = 1.056 \pm 0.005$ mm; and
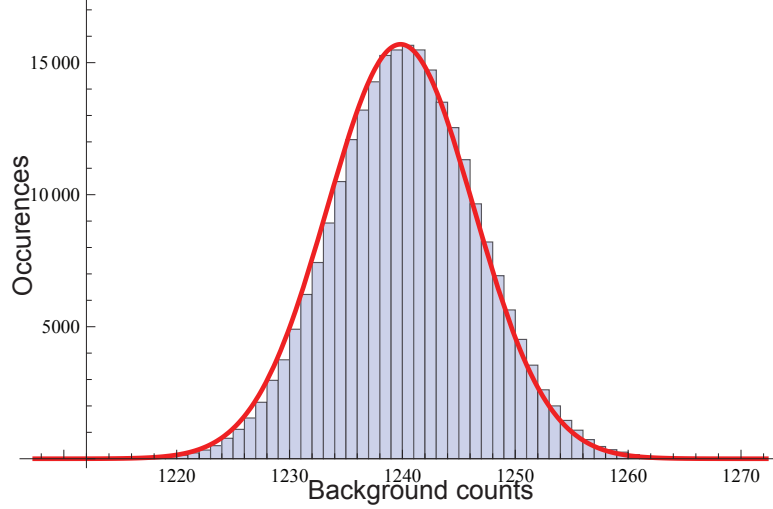
62

Figure 4.3: Histogram of background counts for a single shot image. The 1 std. dev. width of the histogram is 6.48 with central value of 1239.83 counts. Red curve is a Gaussian function. The background appears to be 1.54 standard deviations away from the CCD dark count noise indicating very low background counts.

a commercial device (64) with a calculated refractive index $n = 1.56 \pm 0.02$ (64) and measured step height $\Delta h = 0.93 \pm 0.05$ μm (64), yielding $r_2 = 0.219 \pm 0.008$, $\alpha = 0.94 \pm 0.06$, and $\beta = 5.2 \pm 0.3$. The flat face of the device is mounted on a borofloat glass substrate ($n \approx 1.47$). The refractive index is calculated from the dispersion equation in Eq. A.1 of appendix A, with the uncertainty estimated from the wavelength dependence of the dispersion equation. The uncertainty in the step height is provided by the phase plate etalon manufacturer. The pitched face of the device and opposing surface of the substrate are exposed to air ($n \approx 1.00027$).

The experimental set-up consist of a single lens imaging system with the spiral phase plate etalon (CCD) placed 2 focal lengths before (after) the lens as shown in Fig. 4.4(b), with a numerical aperture of NA ≈ 0.08. The purpose of the imaging system is to probe the intensity pattern immediately after the spiral phase plate etalon, i.e. the diffraction near field. Without the imaging lens, a vortex core emerges as the beam propagates far away (diffraction far field) from the spiral phase plate
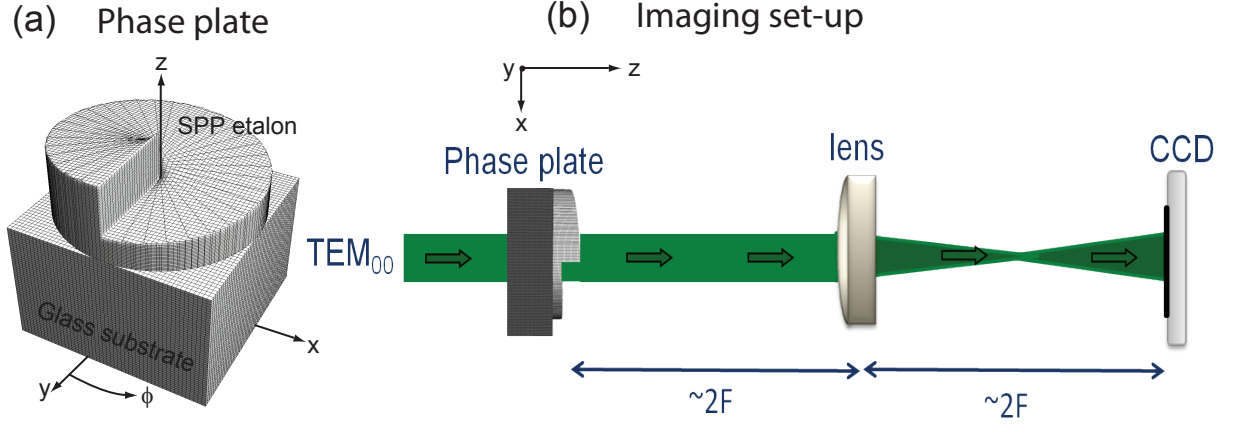
Figure 4.4: (a) Spiral phase plate etalon. (b) Imaging set-up (Not drawn to scale). A TEM$_{00}$ Gaussian beam coming out from a single mode optical fiber propagates through a spiral phase plate etalon with a 1 lens system to image the optical beam immediately after the spiral phase plate etalon onto the CCD camera. In other words, the 1 lens imaging system is used to probe the diffraction near field of the spiral phase plate etalon. The numerical aperture of the imaging lens is NA$=\frac{D}{2F} \approx 0.08$. $D = 25.4$mm is the diameter of the lens and $F = 150$mm is the focal length of the lens.

etalon for integer winding number (e.g. $\alpha = 1$, 2, 3, etc) (13; 14; 24; 32; 53), and for the case of non-integer winding number (e.g. $\alpha = 0.5$, 1.5, 2.5, etc), a vortex core and region of zero intensity in an azimuthal angle on the optical intensity profile emerges (10; 11; 12; 19; 49; 50; 51). Here, $\alpha = 0.94$ which is very close to 1, and therefore the beam will have a ring (or donut) intensity profile in the far field. The work in this chapter is focused on probing and analyzing multiple beam interference effects in the diffraction near field of the device with the set-up shown in Fig. 4.4(b).

4.2.3 Experimental data and analysis

In the experiment, 280 frames of four set of images are taken on the CCD: Gaussian laser beam without the spiral phase plate etalon present to characterize the optical intensity profile on the input plane of the device [Fig. 4.5(c)], a first background counts image [Fig. 4.5(e)], Gaussian laser beam after propagation through the spiral phase plate etalon to characterize the optical intensity profile on the output plane
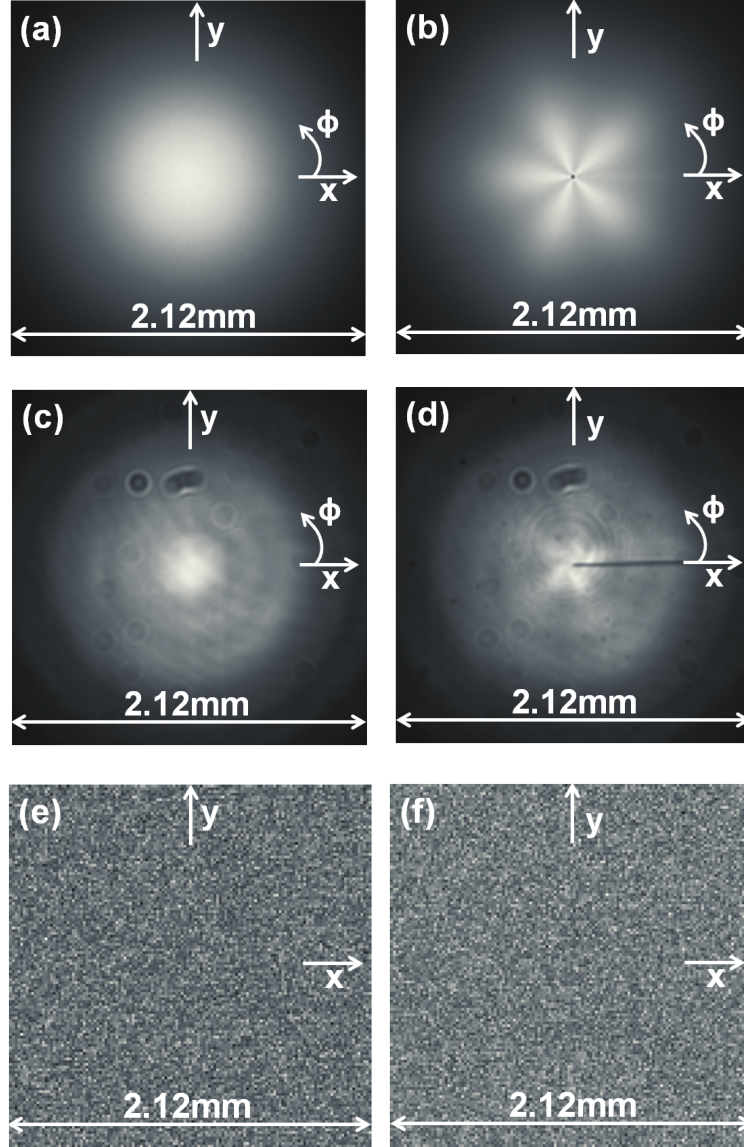
Figure 4.5: Optical transmission through a spiral phase plate etalon. Computer generated optical intensity profile based on shot noise limited assumptions on the input plane (a), and output planes (b) of the device. The corresponding experimental optical intensity profile at the input (c) and output (d) planes of the device. The input optical intensity profile has $I(r, \phi, 0) \propto e^{-2r^2/\omega_0^2}$ (Gaussian intensity profile) and the output intensity profile has $I(r, \phi, h_0 + \Delta h) \propto T(\phi)e^{-2r^2/\omega_0^2}$ (Optical vortex intensity profile). The dark horizontal line in (d) is due to the sudden change in material thickness at $\phi = \{0, 2\pi\}$ [as seen in Fig. 4.4 (a)]. (e) First experimental background count image to subtract from Gaussian laser beam background offset and (f) Second experimental background count image to subtract from optical vortex beam background offset.

2D profile **Raw data** **Binned data**

(a) (c) (e)

(b) (d) (f)

2.12mm

$T(\phi)$, ϕ/π [rad]

(c)

	Estimate	Standard Error	Confidence Interval
$A^{CalcFit}$	0.999525	0.000186543	{0.999338, 0.999712}
$r_2^{CalcFit}$	0.219025	0.00016723	{0.218858, 0.219193}
$\beta^{CalcFit}$	5.22126	0.000907048	{5.22035, 5.22217}
$\phi_0^{CalcFit}$	0.915084	0.000346422	{0.914738, 0.915431}

(e)

	Estimate	Standard Error	Confidence Interval
$A^{CalcFit}$	0.999331	0.000173943	{0.999156, 0.999505}
$r_2^{CalcFit}$	0.21882	0.000155821	{0.218664, 0.218977}
$\beta^{CalcFit}$	5.22134	0.000845472	{5.22049, 5.22219}
$\phi_0^{CalcFit}$	0.915001	0.000322575	{0.914677, 0.915325}

(d)

	Estimate	Standard Error	Confidence Interval
A^{Fit}	1.0676	0.000733686	{1.06687, 1.06834}
r_2^{Fit}	0.20647	0.00064234	{0.205827, 0.207113}
β^{Fit}	5.01384	0.00338839	{5.01045, 5.01723}
ϕ_0^{Fit}	0.0429454	0.000794202	{0.0421507, 0.0437402}

(f)

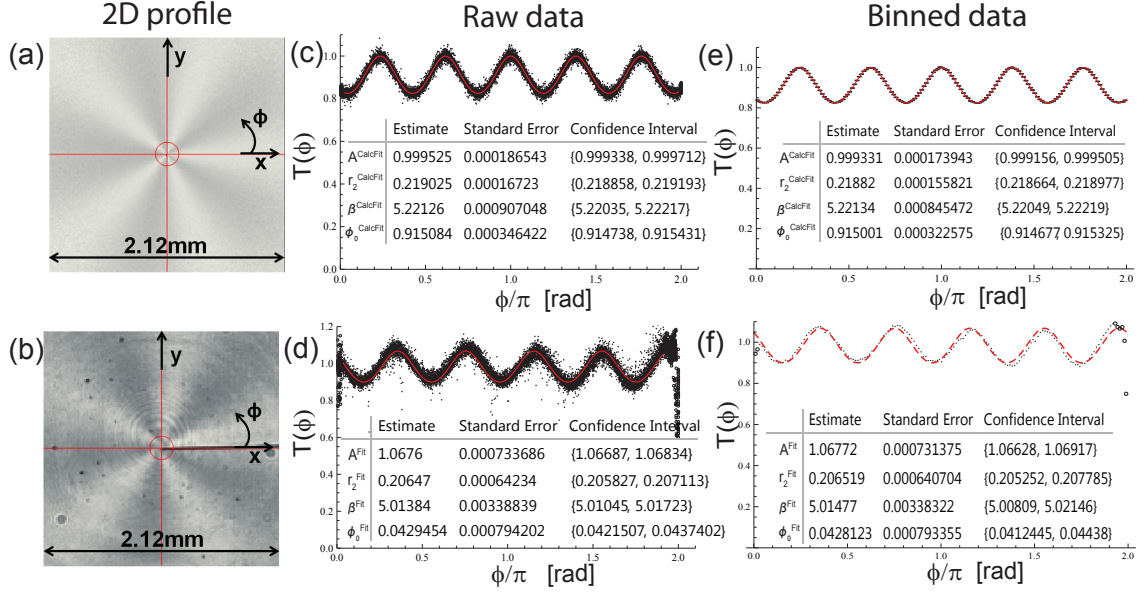|	Estimate	Standard Error	Confidence Interval
A^{Fit}	1.06772	0.000731375	{1.06628, 1.06917}
r_2^{Fit}	0.206519	0.000640704	{0.205252, 0.207785}
β^{Fit}	5.01477	0.00338322	{5.00809, 5.02146}
ϕ_0^{Fit}	0.0428123	0.000793355	{0.0412445, 0.04438}

Figure 4.6: 2D optical vortex intensity profile on output plane of device based on shot noise limited assumptions normalized with Gaussian beam on input plane of device for (a) computer generated data, and (b) Experimental data. The red cross bar in the 2D profile is used to find the center of the normalized beam profile in order to plot the transmission function, $T(\phi)$, as a function of azimuthal angle, ϕ, in (c) and (d) for the raw data, and (e) and (f) for binned data. The images in (a) and (b) are divided into $a = 160$ angular wedges [i.e. $a = 160$ bins] and the transmittance is calculated for each angular wedge from Eq. 4.3 to give (e) and (f), respectively. The data affected by the dark horizontal line in (b) and Fig. 4.5(d) are plotted as open circles and excluded from the fit. The single image fit parameters are in the inset of the raw and binned data plots. The 68% confidence interval is reported by the fit routine. By comaping the single image fit parameters of the computer generated data and experimental data, it can be seen that the error on the experimental fit parameters is within a factor of 5 of the error on the computer generated shot noise limited fit parameters. An alternative way of obtaining the single image error bar is in Fig. 4.8, which produces similar results as a single image analysis output from a built-in Mathematica fit routine in the inset of (e) and (f).
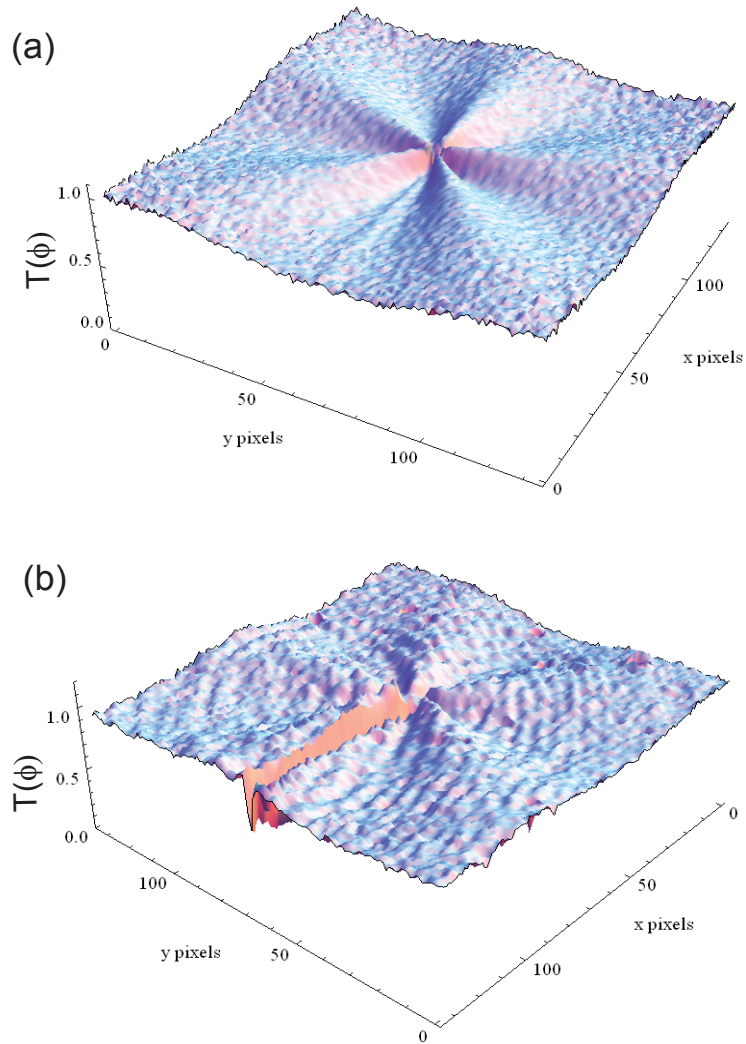
Figure 4.7: 3D plot of optical vortex normalized with Gaussian laser beam integrated out to the $\frac{1}{e^2}$ beam radius for the Computer generated data (a), and Experimental data (b). The dip in the intensity pattern in (b) is due to the sudden change in material thickness at $\{0, 2\pi\}$ of the spiral phase plate etalon shown in Fig. 4.4 (a).

of the device, i.e. optical vortex laser beam [Fig. 4.5(d)], and a second background count image [Fig. 4.5(f)]. There is an offset in the CCD background per pixel of approximately 10^3 counts and fluctuating with a 1 std. dev. width of approximately 7 counts (See fig. 4.3).

The experimental transmittance for each CCD pixel is computed as

$$T_i = \frac{N_{V_i} - N_{BV_i}}{N_{G_i} - N_{BG_i}}. \tag{4.1}$$

N_{V_i}, N_{BV_i}, N_{G_i} and N_{BG_i} are the single pixel count for the optical vortex laser beam on the output plane of the spiral phase plate etalon, optical vortex laser beam background, Gaussian laser beam without the spiral phase plate etalon present on the input plane of the device, and Gaussian laser beam background, respectively. The subscript i is used to denote the ith pixel. The random statistical error on each pixel is

$$|\delta T_i|^2 = \left(\frac{\partial T_i}{\partial N_{V_i}} \delta N_{V_i} \right)^2 + \left(\frac{\partial T_i}{\partial N_{BV_i}} \delta N_{BV_i} \right)^2 + \left(\frac{\partial T_i}{\partial N_{G_i}} \delta N_{G_i} \right)^2 + \left(\frac{\partial T_i}{\partial N_{BG_i}} \delta N_{BG_i} \right)^2 \tag{4.2}$$

where δN_{V_i}, δN_{BV_i}, δN_{G_i} and δN_{BG_i} is the single pixel standard deviation of the 280 frames taken for the optical vortex laser beam counts, optical vortex background counts, Gaussian laser beam counts, and Gaussian laser beam background, respectively. For each pixel, a weight $w_{T_i} = \frac{1}{\delta T_i^2}$ is computed, and an angle ϕ_i is assigned. The vortex beam frames normalized with Gaussian beam frames in Fig. 4.6(b) are divided into $a = 160$ angular wedges as seen in Fig. 4.6(f). A circle of radius 80μm is removed from the center of the beam as this corresponds to the part of the beam for which there is no periodic modulation in the experimental frames [See fig. 4.6(b)]. The transmittance is computed for each angular wedge as the weighted average of k

pixels in that particular wedge:

$$T_a\left(\phi\right) = \frac{\sum_{i=1}^{k} T_i w_{T_i}}{\sum_{i=1}^{k} w_{T_i}}. \tag{4.3}$$

The weight of each angular wedge is $w_a = \sum_{i=1}^{k} w_{T_i}$, which goes into the least square fitting routine. In this chapter, the index "a" represents the ath angular wedge of the transmission function,

$$T(\phi) = \frac{A^{\mathrm{Fit}}}{1 + \frac{4|r_2^{\mathrm{Fit}}|^2}{(1-|r_2^{\mathrm{Fit}}|^2)^2} \sin^2\left(\frac{\beta^{\mathrm{Fit}}(\phi+\phi_0^{\mathrm{Fit}})}{2}\right)}, \tag{4.4}$$

A^{Fit} and r_2^{Fit} is the peak of the transmission function and its modulation depth, respectively. β^{Fit} and ϕ_0^{Fit} is the modulation frequency and position of the transmission function , respectively, with $\phi_0^{\mathrm{Fit}} \in \{0, 2\pi\}$. It should be noted that ϕ_0^{Fit} could be any real number, but since it represents the position of the angular interference pattern, it is normalized to a value between 0 and 2π. The fitting routine calculates a value of χ^2 that minimizes the sum of deviations of the experimental data from the transmission function,

$$\chi^2 = \sum_a w_a \left[T_a\left(\phi\right) - T\left(\phi_a\right)\right]^2, \tag{4.5}$$

$T_a\left(\phi\right)$ and $T\left(\phi_a\right)$ is the ath angular wedge of the experimental and calculated transmission function, respectively, and computed from Eq. 4.3 and Eq. 4.4, respectively. w_a is the weight of the ath angular wedge. A weighted fit to the experimental data enables the program to determine the single image experimental fit parameters [shown in the inset of Fig. 4.6(d) and (f)] to greater precision, with a lower limit given by the shot-noise limited values [shown in the inset of Fig. 4.6(c) and (e)].

While only one frame is shown in Fig. 4.5(c), Fig. 4.5(d), Fig. 4.5(e), and Fig. 4.5(f) for the Gaussian laser beam counts, optical vortex beam counts, and two sets of background counts, respectively, 280 of such frames are taken. Each set of these

frames is computed from Eq. 4.1, binned into angular wedges according to Eq. 4.3, and fit to Eq. 4.4 by minimizing χ^2 in Eq. 4.5. An example of a single fit to the experimental transmittance is in Fig. 4.6(d) and (f). A histogram is made for each of the fit parameters (A^{Fit}, r_2^{Fit}, β^{Fit}, and ϕ_0^{Fit}) as shown in Fig. 4.8(e)-(h). The single frame uncertainty is the 1 std. dev. width (68% confidence interval) of the fit parameter distribution.

The experimental transmitted optical intensity displays a periodic modulation as a function of azimuthal angle [Fig. 4.6(b), (d) and (f)]. The observed peak of the transmission function is $A^{\mathrm{Fit}} = 0.99 \pm 0.07$ and agrees with the expected value of $A = 1$ to within 0.48% (~ 0.095 std. dev. in units of the experimental error bar). The position parameter is $\phi_0^{\mathrm{Fit}} = (0.044 \pm 0.001)\,\pi$, where $\phi_0^{\mathrm{Fit}} \in \{0, 2\pi\}$. The observed modulation frequency, $\beta^{\mathrm{Fit}} = 5.012 \pm 0.003$, agrees with the predicted central value, β, to within 4.01% (~ 0.71 std. dev. in units of calculated error bar). The observed modulation depth yields $r_2^{\mathrm{Fit}} = 0.2067 \pm 0.0004$, which is 5.7% ($\sim 1.66$ std. dev. in units of calculated error bar) below the predicted central value. By incorporating the lower reflectivity of air-substrate interface into the calculations, better agreement between experiment and theory is expected. In addition, the substrate is not expected to modify the predicted modulation frequency, as shown in appendix B.

4.2.4 Computer generated data

A computer model of the optical intensity profile at the input [See fig. 4.5(a)] and output planes [See fig. 4.5(b)] of the device is generated based upon shot noise limited assumptions, i.e. the arrival of photon counts on the CCD detector and background fluctuation in each pixel strictly follows Poisson statistics:

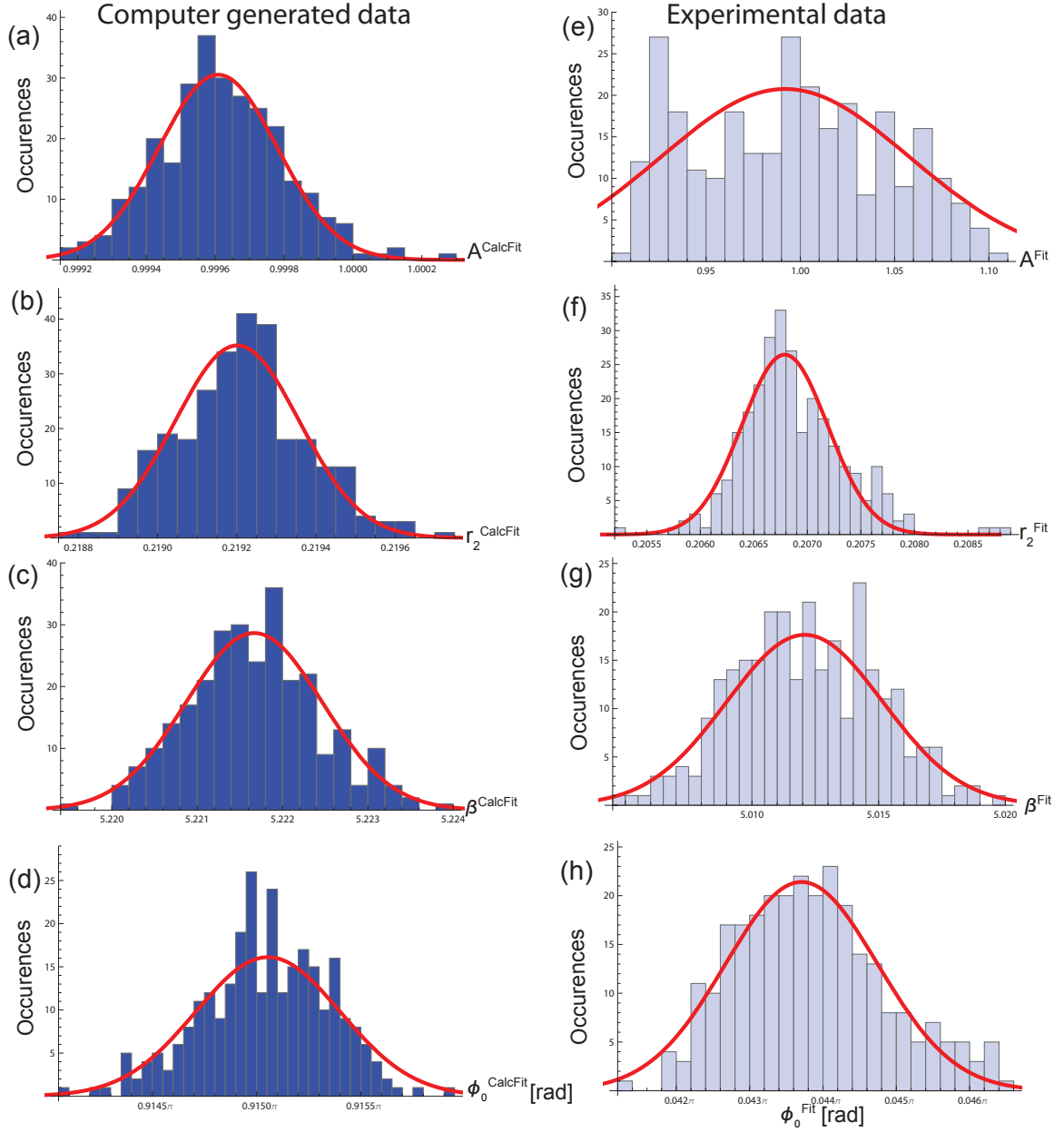$$P\left(\mu, n_c\right) = \frac{\mu^{n_c}}{n_c!}e^{-\mu}. \tag{4.6}$$

Figure 4.8: Histogram of fit parameters shows an approximate Gaussian distribution. The central value and single frame uncertainty (1 std. dev. width of the distribution) for the parameters is shown as follows. *Computer generated data:* (a) $A^{\text{CalcFit}} = 0.9996 \pm 0.0002$, (b) $r_2^{\text{CalcFit}} = 0.2192 \pm 0.0002$, (c) $\beta^{\text{CalcFit}} = 5.2218 \pm 0.0008$, (d) $\phi_0^{\text{CalcFit}} = 0.9150\pi \pm 0.0003\pi$. *Experimental data:* (e) $A^{\text{Fit}} = 0.99 \pm 0.07$, (f) $r_2^{\text{Fit}} = 0.2067 \pm 0.0004$, (g) $\beta^{\text{Fit}} = 5.012 \pm 0.003$, (h) $\phi_0^{\text{Fit}} = (0.044 \pm 0.001)\,\pi$. The uncertainty here is not the fit error on a single image as in the inset of Fig. 4.6(e) and (f) for simulated and experimental data, respectively, but determined from fitting 280 simulated and experimental transmittance. Nevertheless, the values reported by both methods appear to agree to within a factor of two for r_2, β, and ϕ_0 parameters.

71
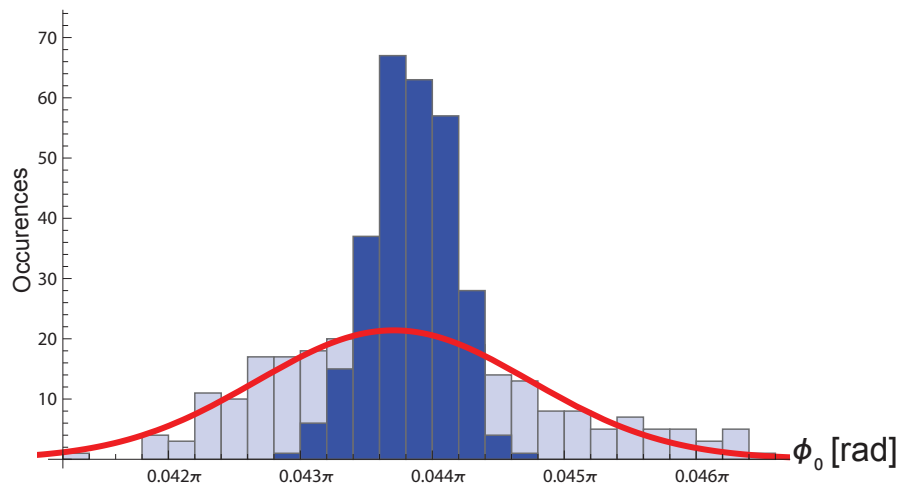
Figure 4.9: Histogram of the angular position fit parameter, ϕ_0, for the shot-noise limited computer generated data (Dark blue) and experimental data (light blue) plotted on the same axis. This plot is the same as the ϕ_0 histogram in Fig. 4.8 (d) and (h), but plotted on the same axis, with an additive normalization factor put on the central value of the computer generated data so that the central value of the two histograms are well overlapped. The red curve is a fit of the experimental histogram to a Gaussian function. The error in the experimental angular position parameter, ϕ_0, appears to be within a factor of 3.04 of the shot noise limited value.

This is the probability of detecting n_c photon counts with mean photon counts, μ arriving at the detector. The mean photon counts of the optical intensity profile at the input plane of the device is $\mu_G = I_0 e^{-2r^2/\omega_0^2}$ [See fig. 4.5(a)] on top of fluctuating background counts, and at the output plane of the device is $\mu_V = I_0 T(\phi) e^{-2r^2/\omega_0^2}$ [See fig. 4.5(b)] on top of fluctuating background counts, where I_0 and ω_0 is the peak count of the optical intensity profile, and $1/e^2$ beam radius, respectively. A random integer generator is used to create the counts in each pixel. Similarly, two sets of fluctuating background counts is generated in order to subtract it from the computer generated optical intensity profile for the Gaussian beam at the input and vortex beam at the output planes of the device. The parameters for generating the optical intensity profile are $r_2 = 0.2193$, $\alpha = 0.939$, and $\beta = 5.2217$. The peak counts for the optical intensity profile is $I_0 = 3.72 \times 10^4$ counts and a $1/e^2$ beam radius of $\omega_0 = 1.06$ mm. An offset in fluctuating CCD background of 1232 counts with 1 std. dev. width of 7 counts is also incorporated in the analysis of the computer generated data.

In the simulation of the data, 280 frames of the optical intensity profile is generated at the input (Gaussian beam) and output planes (vortex beam) of the device. In addition, two sets of background counts is generated, each containing 280 frames. The analysis performed on the experimental data in the previous section is the same analysis performed on the computer generated data. The transmission function through each pixel is computed from Eq. 4.1 and the random statistical error is computed from Eq. 4.2, where in this case the data is shot noise limited, i.e. $\delta N_{V_i} = \sqrt{N_{V_i}}$, $\delta N_{BV_i} = \sqrt{N_{BV_i}}$, $\delta N_{G_i} = \sqrt{N_{G_i}}$ and $\delta N_{BG_i} = \sqrt{N_{BG_i}}$. The frames in Fig. 4.5(a) and Fig. 4.5(b) are divided into 160 angular wedges and the transmittance is computed for each angular wedge from Eq. 4.3 as shown in Fig. 4.6(e). By fitting each of the 280 computer generated transmittance, a histogram of the each of the fit parameters is obtained as shown in Fig 4.8(a)-(d). The fit parameters are $A^{\mathrm{CalcFit}} = 0.9996 \pm 0.0002$

(2.01 std. dev.), $r_2^{\text{CalcFit}} = 0.2192 \pm 0.0002$ (1.12 std. dev.), $\beta^{\text{CalcFit}} = 5.2216 \pm 0.0008$ (0.008 std. dev.), and $\phi_0^{\text{CalcFit}} = (0.9150 \pm 0.0003)\,\pi$. The value in parenthesis is the number of standard deviations that the hand selected parameters used to generate the data differs from the computer generated histograms as seen in Fig 4.8(a)-(d).

4.2.5 Comparison of experimental data and shot-noise limited computer generated data

The central value and uncertainty is obtained by fitting each of the collected 280 frames of the CCD. A sample fit of the experimental optical intensity profile is shown in Fig. 4.6(b). The distribution of experimental fit values for A^{Fit}, r_2^{Fit}, β^{Fit} and ϕ_0^{Fit} is in Fig. 4.8(e)-(h), with single frame value of $A^{\text{Fit}} = 0.99 \pm 0.07$, $r_2^{\text{Fit}} = 0.2067 \pm 0.0004$, $\beta^{\text{Fit}} = 5.012 \pm 0.003$, and $\phi_0^{\text{Fit}} = (0.044 \pm 0.001)\,\pi$. Similarly, the distribution of fit values to the computer generated data for the parameters, A^{CalcFit}, r_2^{CalcFit}, β^{CalcFit} and ϕ_0^{CalcFit}, is in Fig. 4.8(a)-(d) which gives a single frame value of $A^{\text{CalcFit}} = 0.9996 \pm 0.0002$, $r_2^{\text{CalcFit}} = 0.2192 \pm 0.0002$ and $\beta^{\text{CalcFit}} = 5.2216 \pm 0.0008$, and $\phi_0^{\text{CalcFit}} = (0.9150 \pm 0.0003)\,\pi$. Comparing the 1 std. dev. error bar of the experimental fit parameters to the computer generated data provides an estimate of how close the experimental parameters are to its shot-noise limited value. The experimental parameters, r_2^{Fit}, β^{Fit}, and ϕ_0^{Fit} appear to be within 2.03, 3.75, and 3.04 of the shot-noise limited computer generated data, respectively. The width of the experimental amplitude parameter can be wider or narrower depending on the relative fluctuation of the laser beam intensity between the vortex beam and Gaussian beam, and can be normalized to 1 as in Eq. 2.4 of chapter II without loss of generality.

4.2.6 Estimating systematic errors using computer generated data

Systematic errors in the analysis of the experimental data could cause further increase of the uncertainty in the fit parameters. A possible source of systematic errors

	Estimate	Standard Error	Confidence Interval
A^{CalcFit}	0.999382	0.000177924	{0.999203, 0.99956}
r_2^{CalcFit}	0.219052	0.000159189	{0.218892, 0.219212}
β^{CalcFit}	5.22154	0.000863127	{5.22067, 5.2224}
ϕ_0^{CalcFit}	0.915138	0.000329287	{0.914807, 0.915468}

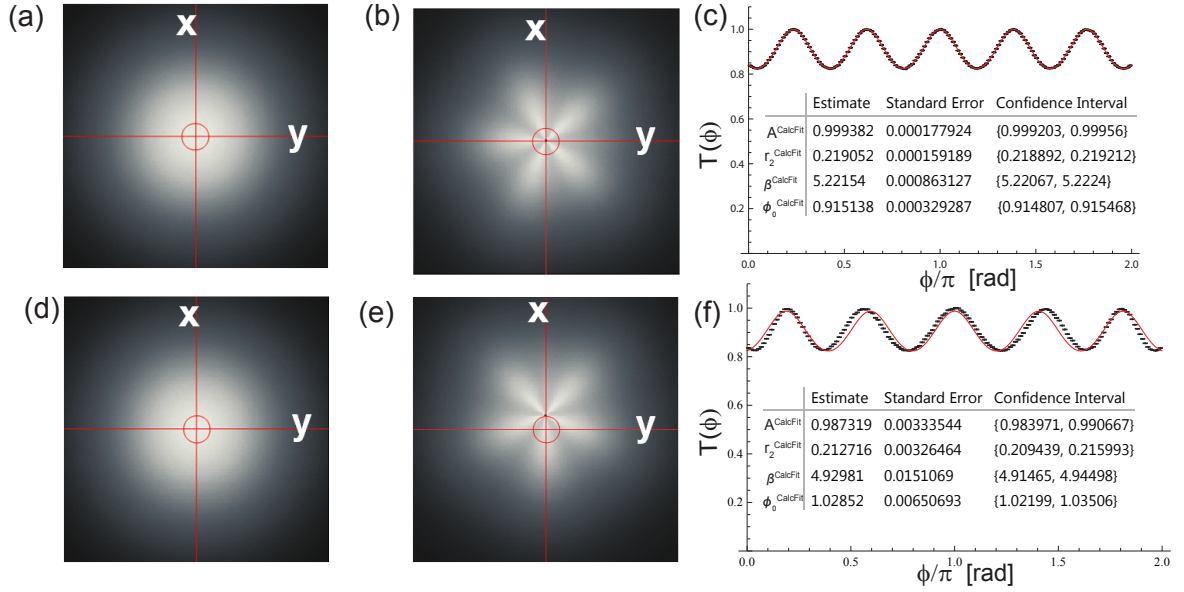|	Estimate	Standard Error	Confidence Interval
A^{CalcFit}	0.987319	0.00333544	{0.983971, 0.990667}
r_2^{CalcFit}	0.212716	0.00326464	{0.209439, 0.215993}
β^{CalcFit}	4.92981	0.0151069	{4.91465, 4.94498}
ϕ_0^{CalcFit}	1.02852	0.00650693	{1.02199, 1.03506}

Figure 4.10: 2D optical intensity profile, and plot of transmission function vs angle for a well centered beam (a)-(c), and an off-centered beam (d)-(f). When the beam is off-centered there will be a systematic shift in the fit parameters. In this case, the optical vortex beam is $r_0 = 7$ pixels away from the center position (black). The red cross bar is used to find the $(x,y)=(0,0)$ [i.e. the $r_0 = 0$] position on the 2D intensity profile. The red curve in the far right column is a single image fit to the computer generated data with the fit parameters in the inset.

may be from improperly determining the center position of the optical intensity profile. The computer generated data is used to quantify this effect by picking positions that are off-centered from the optical intensity profile and making plots of the fit parameters as a function of the radial position away from the center of the optical intensity profile (See fig. 4.11). The amplitude reflectivity, r_2^{CalcFit} decreases by up to 11% and the modulation frequency, β^{CalcFit}, by up to 6.69% for a position that is approximately 7 pixels from the center of the optical intensity profile. Fig. 4.10 contains systematic error analysis of a single image, and Fig. 4.11 contains single image analysis for different off-centered positions of the vortex beam.

When the center position is properly determined, but a circle of radius between 80μm (i.e. 8% of the $1/e^2$ beam waist) and 0.36mm (i.e. 36% of the $1/e^2$ beam
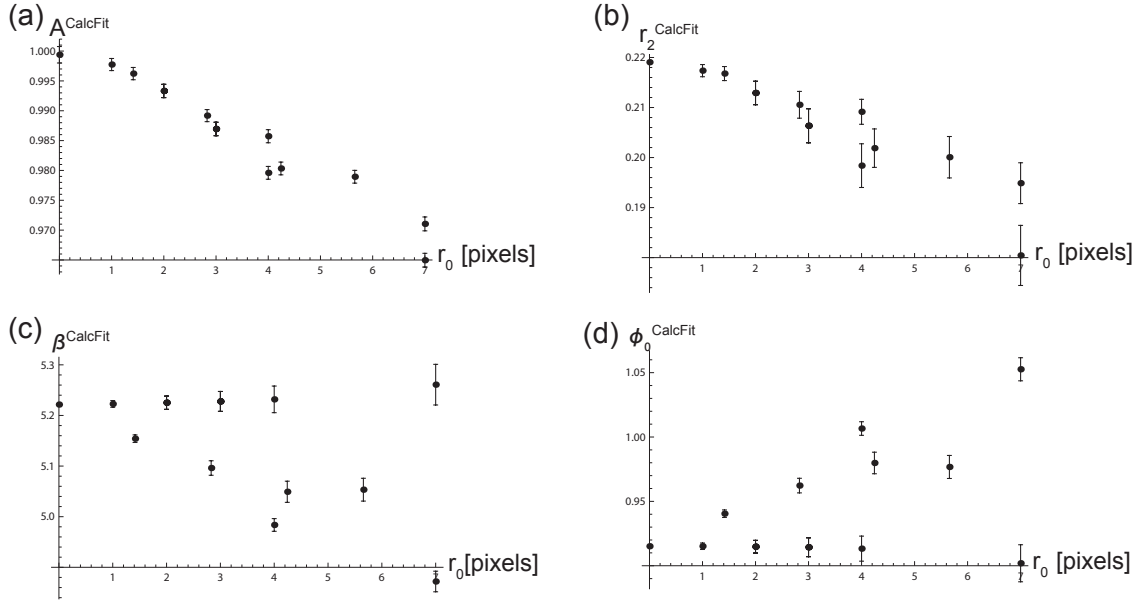
Figure 4.11: Plot show the dependence of the fit parameters on a radial distance, r_0 from the center of the calculated optical intensity profiles. The error bar is determined from a single image fit. In creating the plots above, a radius of 5 pixels is cropped from the middle of the optical intensity profile, since there is no angular modulation in that region for the experimental optical intensity pattern.

waist) is removed from the center of the optical intensity profile, the resulting central value reported by the fitting routine does not appear to be affected to within the single frame 1 std. dev. uncertainty. In the analysis of the experimental data, the center position is chosen to keep possible systematic errors to a minimum. A radius of 80μm is removed from the center of the experimental optical angular interference pattern and so the same is done in the analysis of the computer generated optical intensity profile. Other sources of errors that may contribute to the central value and uncertainty in the experimental fit parameters are distortions in the optical intensity profile.

4.3 Concluding remarks

Multiple beam interference in a spiral phase plate etalon has been measured and compared with analysis of computer generated data based on shot-noise limited assumptions. The measured optical angular intensity arises through interference effects in linear optics. Factors that contribute to random and systematic errors in the data have also been discussed. A major source of random error is the unavoidable shot noise, and a major source of systematic errors is expected to come from finding the center of the optical intensity profile and distortions in the beam profile. The systematic errors are minimized in the experiment by properly overlapping the optical vortex laser beam and Gaussian laser beam, and using the analysis program to find its center. Other sources of errors resulting from dark charge build-up on CCD for long CCD exposure times, electronic noise, background counts,... etc, are negligible. The data has been quantified by a weighted fit to the transmission function, where the central value of the fit parameters describing the spiral phase plate etalon and error bar is obtained. The weighted fit of the experimental data points enables the program to output the experimental fit parameters to a greater precision compared to not weighting the experimental data points. In addition, the output from a mathematica program showing the single image fit parameters and error bar appears to be consistent with the 1 std. dev. width of a histogram generated by minimizing χ^2 for a set of approximately 300 different normalized images. The error on the relevant experimental fit parameters (r_2^{Fit}, β^{Fit}, and ϕ_0^{Fit}) appears to be within a factor of 5 of the shot noise limited value (r_2^{CalcFit}, β^{CalcFit}, and ϕ_0^{CalcFit}).

CHAPTER V

Rotation of an optical angular interference pattern in a spiral phase plate etalon

5.1 Introduction

In this chapter, transmission through a spiral phase plate etalon with changing laser frequency is studied experimentally and compared with theory and computer generated data based on shot-noise limited assumptions. The optical angular interference pattern emerging from the etalon is observed to rotate as the laser frequency is varied and quantified. While the basic properties of the spiral phase plate etalon has been described in chapter II, and analytic tools developed in chapter III, this chapter is focused on a direct application of the device for optical metrology. Such a spiral phase plate etalon may have the potential to play important roles as transverse optical mode filters, and in designing new laser locking and stabilization systems which rely on the ability to accurately measure the rotation (displacement) of the optical angular interference pattern.

These patterns can also form the basis for ultra-stable angular optical lattices to control the rotation dynamics of atoms and micro-particles in the thermal and ultra-cold state. This rotating optical lattice may find applications for building compact inertial sensors and navigation systems such as very sensitive all optical gyroscopes,

as well as in the building blocks of new quantum information processing hardware. In order to use the spiral phase plate etalon for these potential applications, a detailed understanding of the dependence of the phase and amplitude parameters of the angular interference pattern on the laser frequency is required. This will aid in tracking phases (e.g. dynamic or geometric phases) evolving in the device which will ultimately be used in the development of the above mentioned ideas. The spiral phase plate etalon treated in this chapter is an ultra-low finesse device ($F = \frac{\pi r_2}{1-r_2^2} \sim 1$).

5.2 Theory

Some of the theory derived in chapter III is reproduced in this section. In order to elucidate the dependence of the phase on the laser frequency, the transmission function in the thin plate approximation can be written as:

$$T(\phi) = \frac{A}{1 + \frac{4|r_2|^2}{(1-|r_2|^2)^2} \sin^2\left(\frac{\beta(\phi+\phi_0)}{2}\right)} \tag{5.1a}$$

$$= \frac{A}{1 + \frac{4|r_2|^2}{(1-|r_2|^2)^2} \sin^2\left(\frac{\beta\phi+\beta\phi_0}{2}\right)} \tag{5.1b}$$

$$= \frac{A}{1 + \frac{4|r_2|^2}{(1-|r_2|^2)^2} \sin^2\left(\frac{\beta\phi+\frac{2\pi\nu_{Laser}}{FSR}}{2}\right)} \tag{5.1c}$$

$$= \frac{A}{1 + \frac{4|r_2|^2}{(1-|r_2|^2)^2} \sin^2\left(\frac{\beta\phi+\phi_\nu}{2}\right)} \tag{5.1d}$$

r_2 is the reflectivity at the surfaces of the spiral phase plate etalon, β is the modulation frequency of the angular interference pattern (or the number of peaks of the interference pattern), and A is the peak of the interference pattern which is generally normalized to 1. $FSR = \frac{c}{2nh_0}$ is the free spectral range of the etalon, and ν_{Laser} is the center frequency of the laser. Assuming uniform refractive index calculated from the dispersion relation in Eq. A.1 of the appendix and a phase plate base height of $h_0 = 0.6$cm, the free spectral range is $FSR = \frac{3\times10^8}{2\times1.56\times0.6\times10^{-2}} = 16$GHz.

When the laser frequency is changed, there is a change in phase of the transmission function. Any change in phase of the transmission function corresponds to a rotation of the optical angular interference pattern. In other words, as the laser beam makes multiple reflections with the azimuthally varying surface in the spiral phase plate etalon of uniform refractive index, the phase that it acquires is $\varphi_h = \frac{\beta(\phi+\phi_0)}{2} = 2nk\left(h_0 + \Delta h \frac{\phi}{2\pi}\right)$. A change in laser frequency $\delta\nu_{Laser}$ with respect to the center laser frequency ν_{Laser} is equivalent to a small change in etalon transmission function phase, $\delta\varphi_h$, with respect to the total phase acquired by the beam, φ_h,

$$\frac{\delta\nu_{Laser}}{\nu_{Laser}} = \frac{\delta\varphi_h}{\varphi_h}. \tag{5.2}$$

For the device reported in this chapter, the base height, h_0 is engineered such that it is much larger than the azimuthal step height, $h_0 >> \Delta h$, and mathematically the base height does not change with azimuthal angle, $\delta h_0 = 0$, so the fractional change in frequency becomes

$$\frac{\delta\nu_{Laser}}{\nu_{Laser}} = \frac{\Delta h}{h_0} \frac{\delta\phi}{2\pi} \tag{5.3}$$

Hence the interference pattern will rotate by an angle, $\delta\phi$, as a function of a change in frequency $\delta\nu_{Laser}$:

$$\delta\phi = 2\pi \frac{h_0}{\Delta h} \frac{\delta\nu_{Laser}}{\nu_{Laser}}. \tag{5.4}$$

These calculations have assumed that the spiral phase plate etalon is fabricated with uniform refractive index on a glass substrate with the same refractive index, and therefore the rotation angle does not depend on the refractive index. Since the spiral phase plate etalon used in the experiment sits on a glass substrate with different refractive index, the rotation angle vs laser frequency will have a different slope compared to when the glass substrate and spiral phase plate etalon have the same refractive index (See appendix B for further discussion). Furthermore, Eq. 5.4 does not take into account temperature dependent effects which could cause changes in the refractive
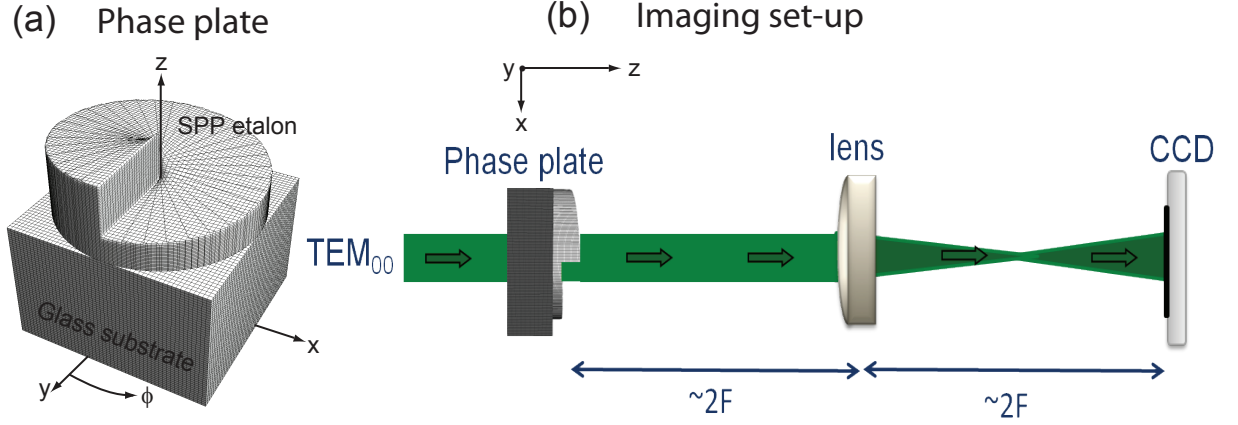
(a) Phase plate

z

SPP etalon

TEM$_{00}$

Glass substrate

y φ x

(b) Imaging set-up

y z

x

Phase plate

lens

CCD

TEM$_{00}$

~2F ~2F

Figure 5.1: (a) Spiral phase plate etalon. (b) Imaging set-up (Not drawn to scale). A TEM$_{00}$ Gaussian beam coming out from a single mode optical fiber propagates through a spiral phase plate etalon with a 1 lens system to image the optical beam immediately after the spiral phase plate etalon onto the CCD camera. In other words, the 1 lens imaging system is used to probe the diffraction near field of the spiral phase plate etalon. The numerical aperture of the imaging lens is NA=$\frac{D}{2F} \approx 0.08$. $D = 25.4$mm is the diameter of the lens and $F = 150$mm is the focal length of the lens.

index or length of etalon, and hence may result in additional changes in rotation of the angular interference pattern on the output plane of the etalon.

5.3   Experiment

The rotation of the optical angular interference pattern as a function of laser frequency is probed using a single lens imaging system with a spiral phase plate placed 2 focal lengths before the lens and the CCD placed two focal lengths after the lens as shown in Fig. 5.1(b). The numerical aperture of the imaging lens is NA $= \frac{D}{2F} \approx 0.08$. The center frequency of the laser is $\nu_{Laser} = 539.384466 \pm 0.0000091$ THz, and $1/e^2$ beam radius, $\omega_0 = 1.065 \pm 0.004$ mm. A commercial spiral phase plate (64) with a calculated refractive index $n = 1.56 \pm 0.02$ (64) and the measured step height is $\Delta h = 0.93 \pm 0.05$ μm (64), yielding $r_2 = 0.219 \pm 0.008$, $\alpha = 0.94 \pm 0.06$, and $\beta = 5.2 \pm 0.3$. The flat face of the device is mounted on a borofloat glass substrate
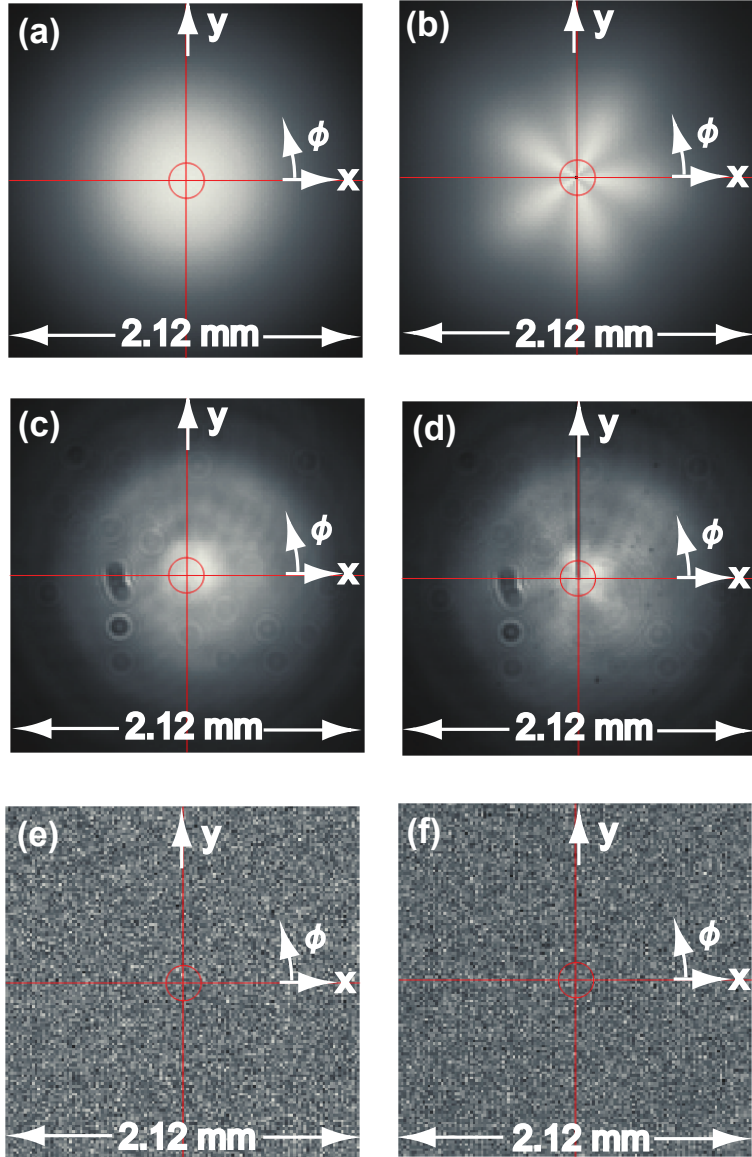
Figure 5.2: Optical transmission through a spiral phase plate etalon. Computer generated optical intensity profile based on shot noise limited assumptions on the input plane (a), and output planes (b) of the device. The corresponding experimental optical intensity profile at the input (c) and output (d) planes of the device. The input optical intensity profile has $I(r, \phi, 0) \propto e^{-2r^2/\omega_0^2}$ (Gaussian intensity profile) and the output intensity profile has $I(r, \phi, h_0 + \Delta h) \propto T(\phi)e^{-2r^2/\omega_0^2}$ (Optical vortex intensity profile). The dark horizontal line in (d) is due to the sudden change in material thickness at $\phi = \{0, 2\pi\}$ [as seen in Fig. 5.1 (a)]. (e) First experimental background count image to subtract from Gaussian laser beam background offset and (f) Second experimental background count image to subtract from optical vortex beam background offset.

2D profile Raw data Binned data

(a) (f) (k)

$\nu_{Laser}=539.387\,750\,\text{THz}$

	Estimate	Standard Error	Confidence Interval
$A^{CalcFit}$	0.999768	0.000160786	{0.999606, 0.999929}
$r_2^{CalcFit}$	0.219203	0.000143717	{0.219059, 0.219348}
$\beta^{CalcFit}$	5.21899	0.000778286	{5.21821, 5.21977}
$\phi_0^{CalcFit}$	0.529235	0.000242523	{0.528991, 0.529478}

(b) (g) (l)

$\nu_{Laser}=539.386\,607\,\text{THz}$

	Estimate	Standard Error	Confidence Interval
$A^{CalcFit}$	0.999404	0.000169886	{0.999234, 0.999575}
$r_2^{CalcFit}$	0.219066	0.00015266	{0.218913, 0.21922}
$\beta^{CalcFit}$	5.21856	0.000804665	{5.21775, 5.21937}
$\phi_0^{CalcFit}$	1.26758	0.000361897	{1.26722, 1.26795}

(c) (h) (m)

$\nu_{Laser}=539.384\,466\,\text{THz}$

	Estimate	Standard Error	Confidence Interval
$A^{CalcFit}$	0.999632	0.00016877	{0.999463, 0.999802}
$r_2^{CalcFit}$	0.219257	0.000154588	{0.219102, 0.219412}
$\beta^{CalcFit}$	5.21767	0.000745296	{5.21692, 5.21842}
$\phi_0^{CalcFit}$	1.21536	0.00032863	{1.21503, 1.21569}

(d) (i) (n)

$\nu_{Laser}=539.382\,405\,\text{THz}$

	Estimate	Standard Error	Confidence Interval
$A^{CalcFit}$	1.	0.00016551	{0.999837, 1.00017}
$r_2^{CalcFit}$	0.219302	0.000153832	{0.219148, 0.219457}
$\beta^{CalcFit}$	5.2187	0.000760823	{5.21794, 5.21946}
$\phi_0^{CalcFit}$	0.39782	0.000220151	{0.397599, 0.398041}

(e) (j) (o)

$\nu_{Laser}=539.381\,424\,\text{THz}$

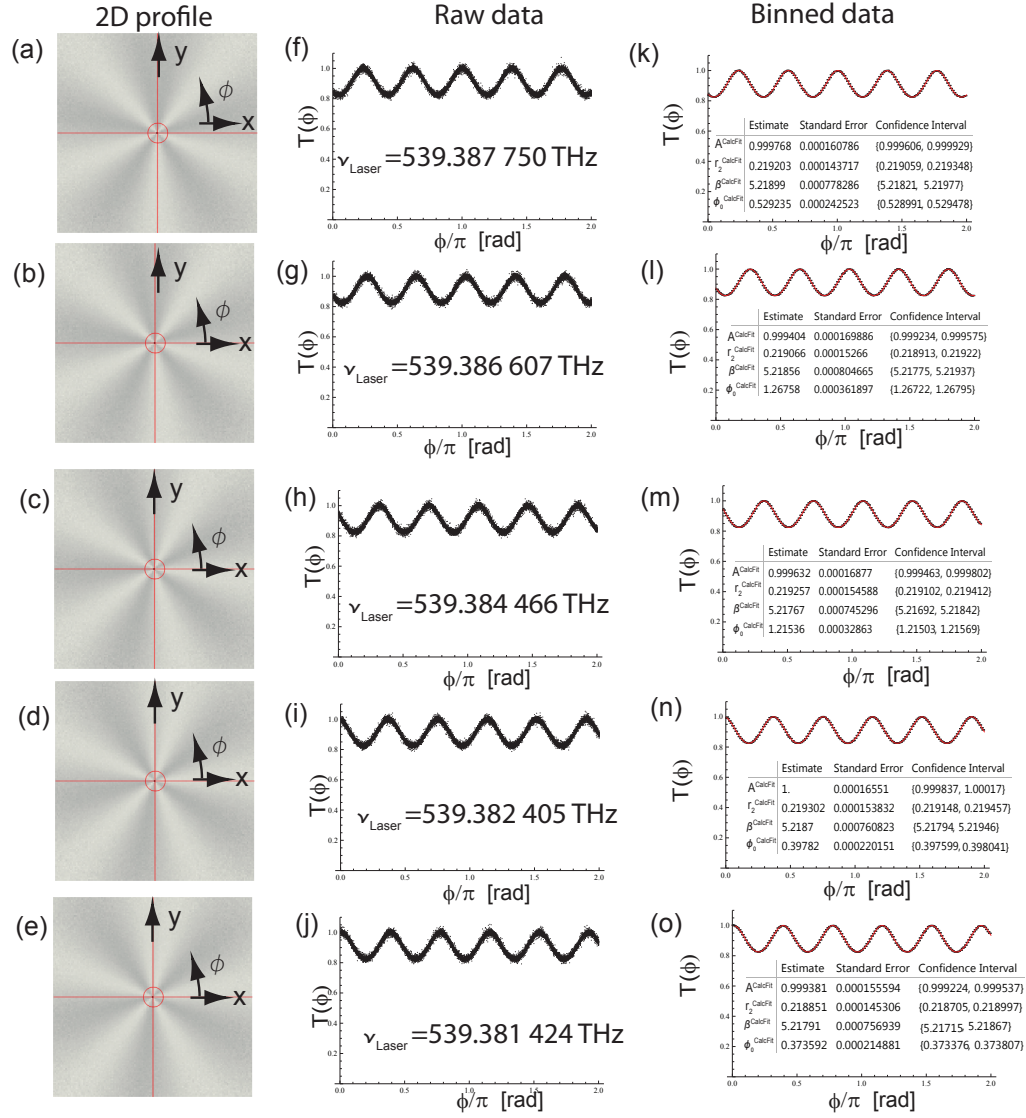|	Estimate	Standard Error	Confidence Interval
$A^{CalcFit}$	0.999381	0.000155594	{0.999224, 0.999537}
$r_2^{CalcFit}$	0.218851	0.000145306	{0.218705, 0.218997}
$\beta^{CalcFit}$	5.21791	0.000756939	{5.21715, 5.21867}
$\phi_0^{CalcFit}$	0.373592	0.000214881	{0.373376, 0.373807}

Figure 5.3: Shot noise limited simulation of experiment, i.e. Computer generated data based on shot noise limited assumptions. (a)-(e): A few selected snap shot normalized 2D images (described by Eq. 3.13 in Chapter III or Eq. 4.1 in Chapter IV) of the angular interference pattern at different laser frequencies showing rotation of the pattern. Red crossbar is to determine center of image and orientation of the angular interference pattern. (f)-(j): Raw data for normalized interference pattern vs angle with corresponding images to left side. (k)-(o): 2D normalized intensity profile binned into 160 angular wedges. Red curve is a single image fit to the simulated transmission function binned into 160 angular wedges, with the fit parameters in the inset. (a), (b), and (c) are selected from the increasing frequency simulation, and (d) and (e) are selected from the decreasing frequency simulation.

2D profile **Raw data** **Binned data**

(a)

(f)

ν_{Laser} =539.387 750 THz

(k)

	Estimate	Standard Error	Confidence Interval
A^{fit}	0.931455	0.000835326	{0.929803, 0.933106}
r_2^{fit}	0.186075	0.000994763	{0.184108, 0.188041}
β^{fit}	5.01556	0.00596437	{5.00377, 5.02735}
ϕ_0^{fit}	0.985451	0.00243503	{0.980637, 0.990266}

(b)

(g)

ν_{Laser} =539.386 607 THz

(l)

	Estimate	Standard Error	Confidence Interval
A^{fit}	1.01841	0.000646063	{1.01713, 1.01969}
r_2^{fit}	0.189275	0.000671978	{0.187947, 0.190604}
β^{fit}	5.01802	0.00415799	{5.0098, 5.02624}
ϕ_0^{fit}	0.545358	0.00133291	{0.542723, 0.547993}

(c)

(h)

ν_{Laser} =539.384 466 THz

(m)

	Estimate	Standard Error	Confidence Interval
A^{fit}	1.1711	0.000968406	{1.16918, 1.17301}
r_2^{fit}	0.20079	0.000808556	{0.199191, 0.202388}
β^{fit}	5.06063	0.00464487	{5.05145, 5.06981}
ϕ_0^{fit}	0.08229	0.00106465	{0.0801854, 0.0843947}

(d)

(i)

ν_{Laser} =539.382 405 THz

(n)

	Estimate	Standard Error	Confidence Interval
A^{fit}	0.892948	0.00109026	{0.890792, 0.895103}
r_2^{fit}	0.202054	0.00118288	{0.199716, 0.204393}
β^{fit}	5.09688	0.00685889	{5.08332, 5.11044}
ϕ_0^{fit}	0.843482	0.00249199	{0.838556, 0.848409}

(e)

(j)

ν_{Laser} =539.381 424 THz

(o)

	Estimate	Standard Error	Confidence Interval
A^{fit}	0.921733	0.000699337	{0.92035, 0.923115}
r_2^{fit}	0.200744	0.000737025	{0.199286, 0.202201}
β^{fit}	5.08647	0.00419773	{5.07817, 5.09477}
ϕ_0^{fit}	0.825401	0.00150003	{0.822435, 0.828366}

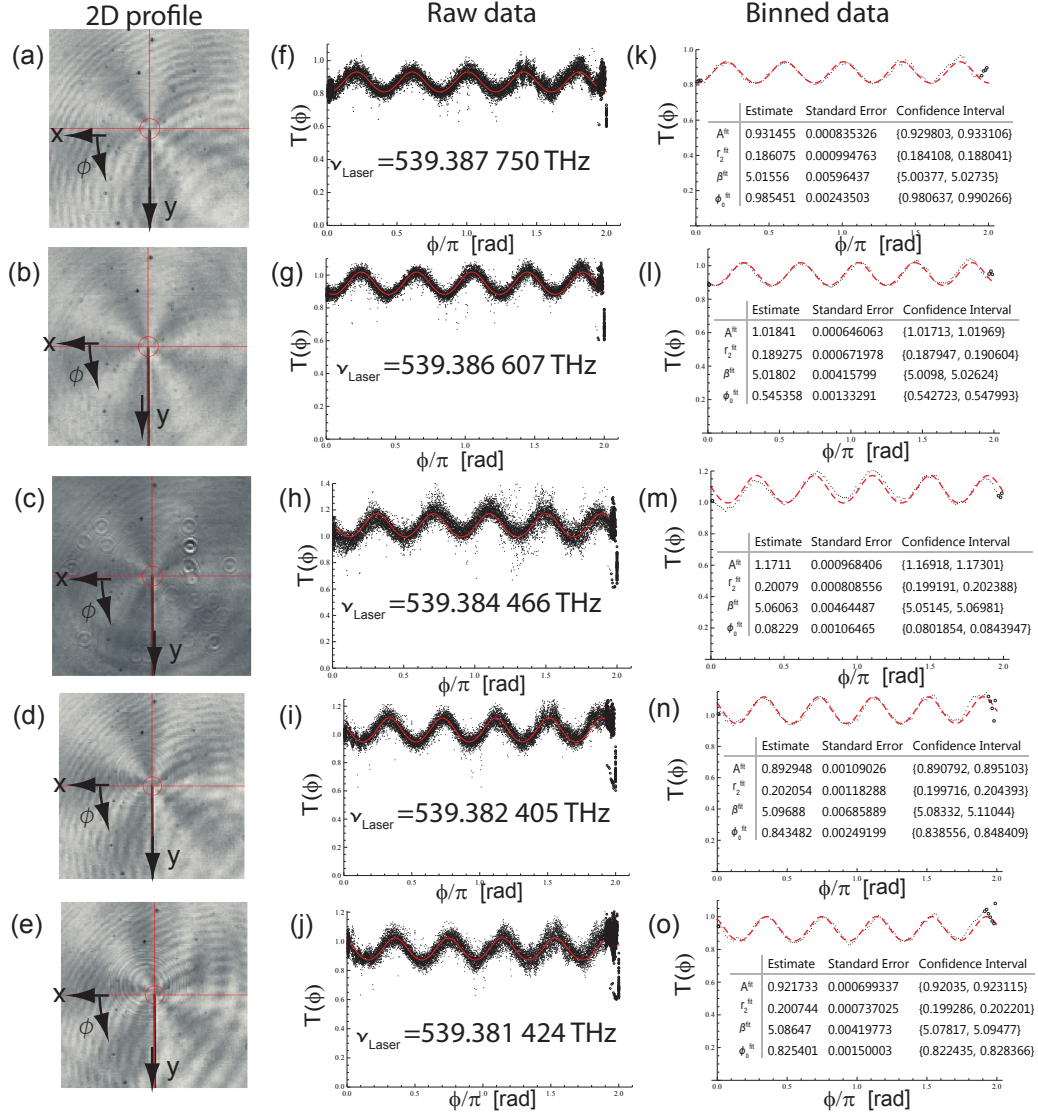Axis labels: $T(\phi)$ vs ϕ/π [rad]

Figure 5.4: Experimental data. (a)-(e): A few selected snap shot normalized (described by Eq. 3.13 in Chapter III or Eq. 4.1 in Chapter IV) 2D images of the angular interference pattern at different laser frequencies showing rotation of the angular pattern. Red crossbar is to determine center of image and orientation of angular interference pattern. The radial fringes in the single shot images is due to etaloning on the CCD camera screen. (f)-(j): Raw data for normalized interference pattern vs angle with corresponding image to left side. Red solid curve is a fit to the raw data. (k)-(0): 2D normalized intensity profile binned into 160 angular wedges. Red dashed curve is a single image fit of the experimental transmittance binned into 160 angular wedges, with the fit parameters in the inset. The circles at the edges are excluded from the experimental fit. (a), (b), and (c) are selected from the increasing frequency measurements, and (d) and (e) are selected from the decreasing frequency measurement.

$(n \approx 1.47)$. The pitched face of the device and opposing surface of the substrate are exposed to air $(n \approx 1.00027)$.

The experimental data analysis performed in this chapter is similar to the analysis performed in chapter IV. Data is taken for an optical vortex beam, Gaussian beam and two sets of background counts. A pixel by pixel normalization is performed according to Eq. 4.1 in chapter IV, and the random statistical error for each data point is computed from Eq. 4.2 in chapter IV. The raw experimental data is binned into 160 angular wedges according to Eq. 4.3 in chapter IV, and a weighted fit is performed to the experimental data by minimizing χ^2 described by Eq. 4.5 in chapter IV. Results from a single image analysis is reported in this chapter. Only a single image analysis is required here because the 1 std. dev. width (fit error bar) of the histograms for the individual fit parameters (r_2^{Fit}, β^{Fit} and ϕ_0^{Fit}) appear to be within 3 std. dev. of the single image fit error bar of the normalized vortex images as shown in chapter IV using a custom fit routine in a Mathematica program. A set of experimental images are taken approximately every 1GHz in the increasing frequency direction and decreasing frequency direction over a frequency window of about 18GHz. This corresponds to a shift in the angular interference pattern from one maximum to the next maximum. In the language of the conventional Fabry-Perot etalon or cavity, this is the free spectral range of the etalon. Fig. 5.4 shows a few selected images of the experimental angular interference pattern, as well as the transmission through the etalon as a function of angle for the raw data and binned data.

5.3.1 Computer generated data

Shot noise limited simulations are performed based on the experimental parameters. The method for generating these simulations is described in section 4.2.3 of chapter IV, and section 3.3 of chapter III. In this case, however, the peak counts for the optical intensity profile is $I_0 = 4 \times 10^4$ counts and the $1/e^2$ beam radius is

$\omega_0 = 1.07$ mm. An offset in fluctuating CCD background of 1232 counts with 1 std. dev. width of 7 counts is also incorporated in the analysis of the computer generated data. The computer generated angular interference pattern is fit to Eq. 5.1(a) were the normalized images, and angular interference patterns are shown in Fig. 5.3. A comparison of the error bar of the single image experimental fit parameters and computer generated data provides an estimate of the shot-noise limit of the experiment. Some of the error on the experimental parameters could be as much as a factor of 12 above the shot noise limited value, but most of the parameters appear to be within a factor of 5 of the corresponding shot-noise limited value. This can be seen by comparing the error on the simulated fit parameters in the inset of Fig. 5.3 to the error on the experimental fit parameters in Fig. 5.4. It must be noted that the spiral phase plate etalon sits on a glass substrate, in which the glass substrate has a different refractive index than the spiral phase plate etalon, and the shot-noise limited computer generated data does not take this into account. A calculation taking this effect into account is in appendix B.

5.3.2 Results and discussion

Measurements of the transmittance through the spiral phase plate is performed as the laser frequency is varied, where the transmission function is characterized by the following parameter: ϕ_0^{Fit}, β^{Fit}, r_2^{Fit}, and A^{Fit}. The angular position ϕ_0^{Fit} and the modulation frequency β^{Fit} quantifies the phase of the transmission function. The reflectivity parameter, r_2^{Fit}, is related to the depth of the modulation (i.e. modulation amplitude) and A^{Fit} is the peak of the normalized angular interference pattern, both of which quantify the amplitudes in the transmission function. All these parameters are determined by fitting the experimental data to Eq. 5.1(a). Identical fit parameters are obtained when the data is fit to Eq. 5.1(d), with the exception of the parameter quantifying the rotation of the optical angular interference pattern, ϕ_ν, which is
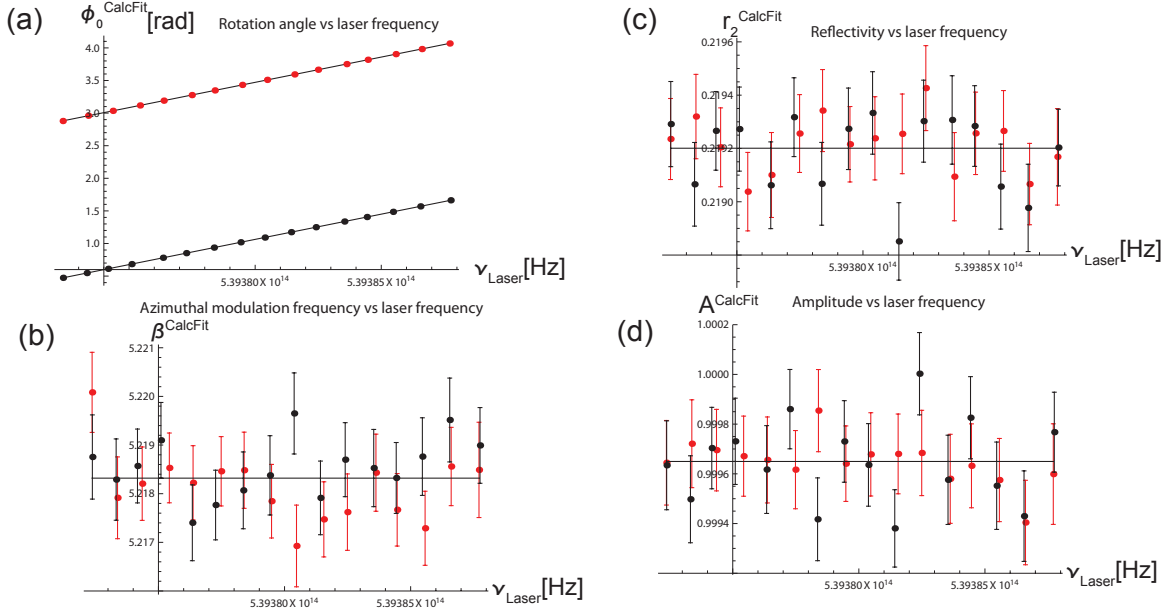
(a) ϕ_0^{CalcFit}[rad]   Rotation angle vs laser frequency

4.0
3.5
3.0
2.5
2.0
1.5
1.0

5.39380 X 10^{14} 5.39385 X 10^{14} ν_{Laser}[Hz]

(c) r_2^{CalcFit} Reflectivity vs laser frequency

0.2196
0.2194
0.2192
0.2190

5.39380 X 10^{14} 5.39385 X 10^{14} ν_{Laser}[Hz]

Azimuthal modulation frequency vs laser frequency

(b) β^{CalcFit}

5.221
5.220
5.219
5.218
5.217

5.39380 X 10^{14} 5.39385 X 10^{14} ν_{Laser}[Hz]

A^{CalcFit} Amplitude vs laser frequency

(d)

1.0002
1.0000
0.9998
0.9996
0.9994

5.39380 X 10^{14} 5.39385 X 10^{14} ν_{Laser}[Hz]

Figure 5.5: Shot-noise limited computer generated single image fit parameters ϕ_0^{CalcFit} (a), β^{CalcFit} (b), r_2^{CalcFit} (c), and A^{CalcFit} (d) for decreasing (black) and increasing (red) laser frequency direction. The computer generated analysis of the data is reported in increasing and decreasing frequency direction because this is the order in which which the data was taken. The laser frequency is varied in the range between 539.372370THz to 539.387710THz. The error bar on the data points for ϕ_0^{CalcFit}, β^{CalcFit}, r_2^{CalcFit}, and A^{CalcFit} are determined from the fitting routine used to fit the computer generated data to the transmission function in Eq. 5.1. The offset in ϕ_0^{CalcFit} between the increasing and decreasing laser frequency direction calculation is because a different fit minimum is used to track the rotation of the pattern. The horizontal black line in β^{CalcFit}, r_2^{CalcFit}, and A^{CalcFit} is the average of both the increasing and decreasing measurements in each plot. The slope of the ϕ_0^{CalcFit} position parameter when the computer generated data is analyzed in the increasing laser frequency direction is $\frac{d\phi_0^{\text{CalcFit}}}{d\nu_{\text{Laser}\oplus}} = (7.736 \pm 0.004) \times 10^{-11}$rad/Hz, and for the decreasing laser frequency direction is $\frac{d\phi_0^{\text{CalcFit}}}{d\nu_{\text{Laser}\ominus}} = (7.747 \pm 0.006) \times 10^{-11}$rad/Hz. The two slope appear to be within $\sim 0.14\%$ (3 std. dev.) of each other, and within 3% of the theory slope calculated from Eq. 5.4. This suggests that the computer program is working properly. The error bar in (a) is smaller than the symbols to represent the data and so it is not visible. This simulation does not take into account the difference in refractive index between the spiral phase plate etalon and glass substrate.
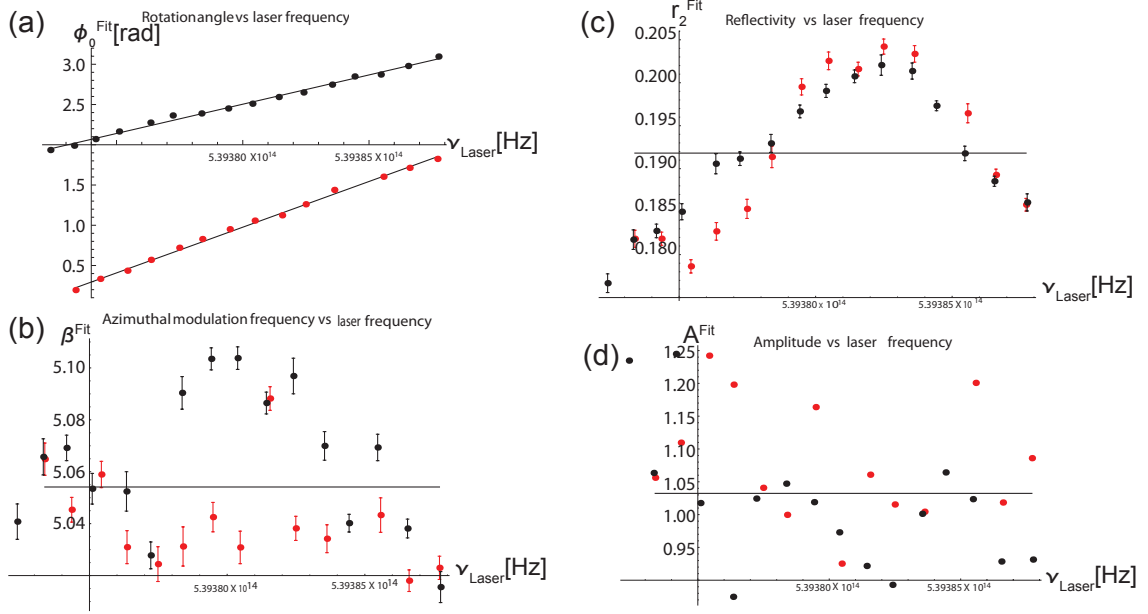
87

(a) ϕ_0^{Fit}[rad] Rotation angle vs laser frequency

3.0

2.5

5.39380 X 10^{14} 5.39385 X 10^{14} ν_{Laser}[Hz]

1.5

1.0

0.5

(b) β^{Fit} Azimuthal modulation frequency vs laser frequency

5.10

5.08

5.06

5.04

5.39380 X 10^{14} 5.39385 X 10^{14} ν_{Laser}[Hz]

(c) r_2^{Fit} Reflectivity vs laser frequency

0.205

0.200

0.195

0.190

0.185

0.180

5.39380 x 10^{14} 5.39385 X 10^{14} ν_{Laser}[Hz]

(d) A^{Fit} Amplitude vs laser frequency

1.25

1.20

1.15

1.10

1.05

1.00

0.95

5.39380 X 10^{14} 5.39385 X 10^{14} ν_{Laser}[Hz]

Figure 5.6: Experimental single image fit parameters ϕ_0^{Fit} (a), β^{Fit} (b), r_2^{Fit} (c), and A^{Fit} (d) for decreasing (black) and increasing (red) laser frequency direction. The analysis is reported in increasing and decreasing frequency direction because this is the order in which the data was taken. The laser frequency is varied in the range between 539.372370THz to 539.387710THz. The error bar on the data points for ϕ_0^{Fit}, β^{Fit}, r_2^{Fit}, and A^{Fit} are determined from the the fitting routine used to fit the experimental data to the transmission function in Eq. 5.1. The horizontal black line in β^{Fit}, r_2^{Fit}, and A^{Fit} is the average of both the increasing and decreasing measurements in that plot. There are more photon counts making position measurements at certain laser frequencies compared to other laser frequencies as seen in the slope of the reflectivity parameter curve. Over a wider laser frequency range, the reflectivity parameter is expected to display a periodic oscillation. The slope of the ϕ_0^{Fit} experimental position fit parameter in the increasing laser frequency direction is $\frac{d\phi_0^{\mathrm{Fit}}}{d\nu_{Laser_\oplus}} = (1.13 \pm 0.02) \times 10^{-10}$rad/Hz, and for the decreasing laser frequency direction is $\frac{d\phi_0^{\mathrm{Fit}}}{d\nu_{Laser_\ominus}} = (0.73 \pm 0.03) \times 10^{-10}$rad/Hz. The two slopes are different by 36% (26 std. dev.) or 56% (128 std. dev.). The error bar for ϕ_0^{Fit} (a) and A^{Fit} (d) is smaller than the symbols to represent the data and so it is not visible.

generally larger than the ϕ_0 parameter (i.e. $\phi_v > \phi_0$). As the laser frequency is changed, the phase of the transmission function changes which induces a rotation of the optical angular interference pattern. This is seen by keeping track of the phase parameters ϕ_0^{Fit} and β^{Fit}, for different laser frequencies through a fit of the data to the transmission function of the spiral phase plate etalon. Fig 5.6 shows the dependence of the experimental fit parameters on laser frequency.

As shown in Fig 5.6(c), the reflectivity parameter, r_2^{Fit}, as a function of laser frequency is a periodic oscillation with one peak displayed (See appendix B for corresponding theory plot), unlike the relatively flat line expected from the simulations shown in Fig. 5.5(c). This indicates that there are more photon counts in the spiral phase plate etalon making position measurements on the CCD at certain laser frequencies compared to other laser frequencies, and is a measure of the longitudinal modes in the etalon. The reflectivity parameter derived from fitting the optical angular interference pattern could also serve as a measure of the etalon finesse or quality factor of the device since it directly quantifies the number of photon counts in the spiral phase plate etalon. The reason for there being more photon counts in the device making position measurements on the CCD at certain laser frequencies compared to other laser frequencies is because the spiral phase plate sits on a glass substrate with different refractive index compared to the material used to fabricate the spiral phase plate . This glass substrate leads to additional interference effects which affects the amplitude parameters (A^{Fit} and r_2^{Fit}) of the resulting fit. However, it does not affect the angular interference pattern modulation frequency, β^{Fit}. Appendix B contains a discussion of these items, which qualitatively agree with the experiment.

The ϕ_0^{Fit} parameter appears to have a linear dependence on the laser frequency as predicted in Eq. 5.4. A linear fit to the angular position, ϕ_0, is performed, where the slope of the line is $\frac{d\phi_0^{\text{Fit}}}{d\nu_{Laser}} = 2\pi \frac{h_0}{\Delta h} \frac{1}{\nu_{Laser}}$. The analysis of the experimental data is reported in increasing and decreasing frequency direction because this is the order

in which the experimental data was taken. The experimental slope for data taken in the increasing laser frequency direction is $\frac{d\phi_0^{\text{Fit}}}{d\nu_{Laser_\oplus}} = (1.13 \pm 0.02) \times 10^{-10}$rad/Hz, and for the decreasing laser frequency direction is $\frac{d\phi_0^{\text{Fit}}}{d\nu_{Laser_\ominus}} = (0.73 \pm 0.03) \times 10^{-10}$rad/Hz, where the error bar reported here is from the linear fit routine. This is a 36% (26 std. dev.) or 56% (128 std. dev.) difference in the slope of the line for the data taken in the increasing and decreasing laser frequency direction. Similar difference in slopes in found when Eq. 5.1(d) is used to quantify the position parameter ϕ_ν of the data, and fit to a straight line, $\frac{d\phi_\nu^{Fit}}{d\nu_{Laser}} = 2\pi \frac{h_0}{\Delta h} \frac{1}{\nu_{Laser}}$. In the simulation of the shot-noise limited computer generated data, the single image slope in the increasing laser frequency and decreasing laser frequency direction agrees to within $\sim 0.14\%$ (3 std. dev.) as shown in Fig. 5.5(a). This suggests that the analysis program is working properly, and these are physical effects arising from the experimental data. It must also be noted that the shot-noise limited simulations does not take into account the fact that the spiral phase plate etalon sits on a glass substrate that does not have the same refractive index as the spiral phase plate etalon.

The slope calculated from Eq. 5.4 and the spiral phase plate parameters are $\frac{d\phi_0}{d\nu_{Laser}} = (7.51 \pm 0.05) \times 10^{-10}$rad/Hz, where the uncertainty in the calculated slope of the line is derived from adding the error on the phase plate parameters in quadrature. The largest sources of error comes from the uncertainty in the step height and base height of the device. The calculated slope from Eq. 5.4 is 3.3% (0.51 std. dev.) and 33% (8 std. dev.) from the experimental slope when the data is taken for position measurements on the CCD detector in the increasing laser frequency direction and decreasing laser frequency directions, respectively. The shot-noise limited simulated slope agrees with the calculated slope in Eq. 5.4 to within 3%. Thus, the experimental increasing laser frequency slope appears to be consistent with the slope based on shot-noise limited simulations to within 6.37% ($\sim$ 3.18 std. dev.). The increasing frequency slope is also within 3% ($\sim$ 2 std. dev. in units of the calculated fit error

bar) of the calculated slope when the spiral phase plate etalon is on a glass substrate with different refractive index as discussed in appendix B. However, the experimental decreasing frequency slope does not appear to be consistent with the increasing frequency slope as evidenced by the 36% ($\sim$ 26 std. dev.) difference in experimental slopes. It must be noted that it is the absolute value of the theory, simulation and experimental slope that is compared to each other. It is also important to note that it is more appropriate to compare the experiment with the theory consisting of a spiral phase plate etalon on a glass substrate with different refractive index as was done above, and discussed in appendix B. Nevertheless, the shot-noise limited simulations are important in that when a fit is performed on the generated data, it provides an estimate of the error bar of the individual fit parameters.

5.4   Concluding remarks

As this work represents the first studies of rotation of an optical angular interference pattern consisting of a superposition of orbital angular momentum modes in a spiral phase plate etalon, it is interesting to note that while the reflectivity parameter, r_2^{Fit} appear to produce consistent results in the increasing and decreasing laser frequency direction, the position parameter, ϕ_0^{Fit}, appear to have a different slope when it is measured for increasing laser frequencies compared to when it is measured for decreasing laser frequencies. In fact, the slope could differ by more than 56% (128 std. dev.). There does not appear to be a "systematic" error introduced by the Mathematica program written to analyze the experimental data as seen from the analysis of the computer generated shot-noise limited data.

A possible source of the inconsistency between the increasing and decreasing frequency measurements for the phase parameters are the temperature dependences of the refractive index and length of the etalon. Since the longitudinal modes resulting from the glass substrate (length$\sim$ 0.6cm) appear to produce consistent results for in-

creasing and decreasing frequency direction measurements as seen from the frequency dependence of the reflectivity parameter, it shows that the changes in refractive index and/or length of the glass substrate etalon is not statistically significant for this measurement. However, these temperature dependent effects may be statistically significant for the spiral phase plate etalon since the device has feature sizes on the order of a micron and it is fabricated from a different material compared to the glass substrate. The temperature changes close to the device was not measured and it is not clear which polymer was used to fabricate the spiral phase plate etalon. Therefore conclusions cannot be made as to whether this is a plausible cause of the inconsistency in the measurement performed in the increasing and decreasing laser frequency direction. Temperature dependent effects have been seen in various frequency stabilization devices such as a wedge etalon (81) as well as many other micron scale devices (82; 83; 84; 85).

CHAPTER VI

Conclusion and outlook

In conclusion, this dissertation presented the first treatment of multiple beam interference in a spiral phase plate etalon. These effects naturally leads to the creation of a coherent superposition of orbital angular momentum states, which has been studied theoretically in chapter II, and experimentally measured in chapter IV of the dissertation. It has been particularly fascinating studying these effects and exploring possible applications. While the work in the dissertation focused on the manipulation of a classical light beam in an ultra-low finesse spiral phase plate etalon, it will be particularly interesting to extend the work to the high finesse case and study a superposition of orbital angular momentum states when:

1. A classical light beam is transmitted through the etalon and determine whether the device can be made more sensitive to rotation, and

2. A non-classical light beam is transmitted through the etalon and determine the fundamental limits to optical rotation of the angular pattern.

As the spiral phase plate etalon is a compact system and has a cylindrical symmetry, it may be possible to develop ultra-stable and very sensitive rotation sensors such as a compact all optical gyroscopes, as well as new hardware for quantum information science. For this purpose, a measurement of the angular interference pattern

as a function of laser frequency was performed in chapter V. The angular interference pattern was observed to rotate, and the longitudinal modes from the glass substrate was probed. Future work in this direction will be to study the device for absolute laser frequency measurements. These are just a few examples of the amazing possibilities of this device as a useful tool for optical metrology in optics and photonics research. From an atomic and molecular physics perspective, the diffraction near field of the device can be projected onto atoms or molecules in the thermal or ultra-cold state, and the interaction between the orbital angular momentum modes (OAM) of light and the system explored. This includes the interaction between the OAM modes of light and the center of mass motion of the system, or even more subtle couplings to the rotational, vibrational, or electronic degrees of freedom in the system. Interesting dynamics is expected to emerge.

While the experiments and theory in this dissertation has been primarily focused on the study of multiple beam interference effects in a spiral phase plate etalon, I have also extensively studied a variety of other items such as developing coreless counter-rotating optical vortices in a modified Mach-Zehnder interferometer for angular Kapitza-Dirac diffraction of ultra-cold atoms, laser spectroscopy of ytterbium atoms as well as the design and construction of apparatus for making ultra-cold atoms. In the course of working on these experiments, theory and simulations was also developed. A highlight of the work on counter-rotating vortices is that it provided an alternative analysis method to quantitatively obtain the winding number of an optical vortex directly without prior knowledge of the spiral phase plate fabrication parameters, as well as provided simple scaling laws to describe the propagation dynamics of optical vortices. Even though this part of my PhD work is not included in this dissertation write-up, the work was quite enjoyable and led to a number of interesting research findings not present in the current published scientific literature.

In closing, the discoveries presented in this dissertation are the result of a number of unexpected observations made while performing experiments with spiral phase plates, thus reaffirming the fact that when doing science and engineering, it is important to keep an open mind while investigating the various minute details of the work. It may ultimately lead to new and exciting research findings!
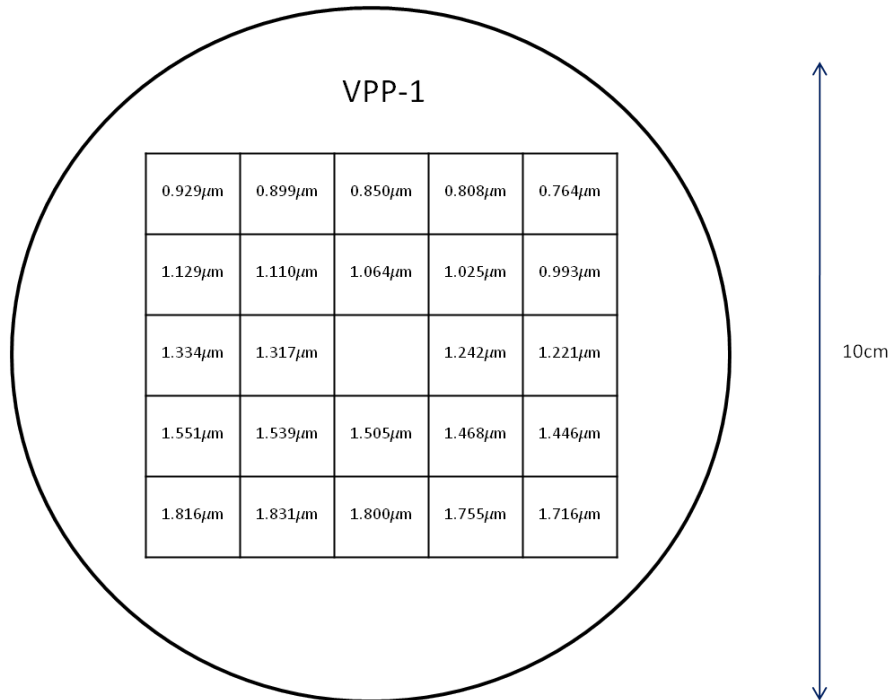
APPENDICES

APPENDIX A

Spiral phase plate geometry

VPP-1

$0.929\mu m$	$0.899\mu m$	$0.850\mu m$	$0.808\mu m$	$0.764\mu m$
$1.129\mu m$	$1.110\mu m$	$1.064\mu m$	$1.025\mu m$	$0.993\mu m$
$1.334\mu m$	$1.317\mu m$		$1.242\mu m$	$1.221\mu m$
$1.551\mu m$	$1.539\mu m$	$1.505\mu m$	$1.468\mu m$	$1.446\mu m$
$1.816\mu m$	$1.831\mu m$	$1.800\mu m$	$1.755\mu m$	$1.716\mu m$

10cm

Figure A.1: Platform consisting of spiral phase plates with different azimuthally vary-
ing thicknesses, Δh, on a glass substrate.

The spiral phase plate sits on a borofloat glass substrate of refractive index $n_g =$
1.470, and it is fabricated by laser writing an azimuthally varying thickness into the

polymer which has the following dispersion equation

$$n_s(\lambda) = 1.5375 + \frac{8290.45}{(\lambda \times 10^9)^2} - \frac{2.11046 \times 10^8}{(\lambda \times 10^9)^4}. \tag{A.1}$$

The units of λ are in m. The platform of spiral phase plates consisting of different azimuthally varying thickness were purchased from RPC photonics (64). The sudden change in material thickness at $\phi_0 = \{0, 2\pi\}$ causes a dark radial line of width on order $20\mu m$ to appear in the intensity profile on the device output plane. Examples of experimental images are in Fig. 4.5(d), Fig. 4.6(b) and Fig. 4.2.3 of chapter IV.
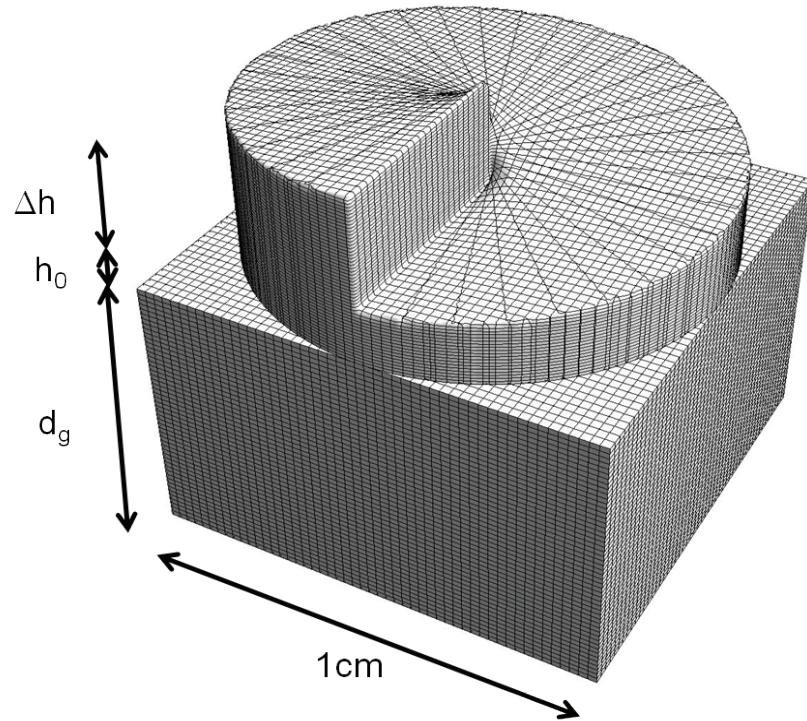
Figure A.2: 3D geometry of a single spiral phase plate with azimuthally varying height Δh, base height h_0, on a glass substrate of thickness d_g.

APPENDIX B

Transfer matrix for wave propagation through a spiral phase plate etalon

The spiral phase plate etalon described in Chapter II and used in the experiments of Chapters IV and V sits on a glass platform with a different refractive index which will ultimately affect the amplitude and phase parameters of the interference pattern on the output plane of the device. In order to take these physical effects into account, the transmission function is computed using the wave transfer matrix formalism in a multi-layered medium (60). The thin plate approximation is assumed in this appendix. The sign convention for the complex electric field amplitude is the same as Chapter II.

For an ideal spiral phase plate etalon with uniform refractive index, the matrix describing the transmission function and reflection function (as in Fig A.2 without the glass substrate) is

$$
\begin{bmatrix} \frac{1}{t^*_{spp}(\phi)} & \frac{r_{spp}(\phi)}{t_{spp}(\phi)} \\ \frac{r^*_{spp}(\phi)}{t^*_{spp}(\phi)} & \frac{1}{t_{spp}(\phi)} \end{bmatrix} = \begin{bmatrix} e^{i\varphi_a} & 0 \\ 0 & e^{-i\varphi_a} \end{bmatrix} \frac{1}{2n_a} \begin{bmatrix} (n_a + n_s)\, e^{+i\varphi_s} & (n_a - n_s)\, e^{-i\varphi_s} \\ (n_a - n_s)\, e^{+i\varphi_s} & (n_a + n_s)\, e^{-i\varphi_s} \end{bmatrix}
$$

$$\frac{1}{2n_s} \begin{bmatrix} (n_s + n_a) & n_s - n_a \\ (n_s - n_a) & (n_s + n_a) \end{bmatrix} \quad \text{(B.1)}$$

$t_{spp}(\phi)$ and $r_{spp}(\phi)$ is the transmission and reflection function of the spiral phase plate etalon, respectively. The third, second and first matrix in Eq. B.1 describes the wave propagation from air to the base of the spiral phase plate etalon, the spiral phase plate etalon to azimuthally varying surface, and the azimuthally varying surface to the constant plane after the azimuthally varying surface, respectively. n_a and n_s is the refractive index of air and the spiral phase plate etalon material, respectively and $\varphi_s = n_s k \left(h_0 + \Delta h \frac{\phi}{2\pi} \right)$ were $k = \frac{2\pi}{\lambda}$. $\varphi_a = n_a k d_a$ were $d_a = \Delta h \left(1 - \frac{\phi}{2\pi} \right)$ is the air gap between the azimuthally varying surface and a uniform plane. After evaluating the matrix, the following is obtained:

$$\frac{1}{t_{spp}(\phi)} = \frac{1}{4n_a n_s} \left\{ (n_a - n_s) e^{+i\varphi_s} e^{+i\varphi_a} (n_s - n_a) + (n_a + n_s) e^{-i\varphi_s} e^{-i\varphi_a} (n_s + n_a) \right\}$$

$$\text{(B.2)}$$

Rearranging the terms in B.2 reproduces Eq. 2.3 in chapter II,

$$t_{spp}(\phi) = \frac{\frac{4n_a n_s}{(n_a + n_s)^2 e^{+i\varphi_a} e^{+i\varphi_s}}}{1 - \left(\frac{n_s - n_a}{n_s + n_a} \right)^2 e^{+2i\varphi_s}} = \frac{t_2 t_1 t_0 e^{+i\alpha\phi}}{1 - r_2^2 e^{+i\beta(\phi + \phi_0)}} \quad \text{(B.3)}$$

When a glass substrate of thickness d_g and different refractive index n_g as in Fig. A.2 is included in the calculation, the transfer matrix becomes:

$$\begin{bmatrix} \frac{1}{t^*_{sppgs}(\phi)} & \frac{r_{sppgs}(\phi)}{t_{sppgs}(\phi)} \\ \frac{r^*_{sppgs}(\phi)}{t^*_{sppgs}(\phi)} & \frac{1}{t_{sppgs}(\phi)} \end{bmatrix} = \begin{bmatrix} e^{+i\varphi_a} & 0 \\ 0 & e^{-i\varphi_a} \end{bmatrix} \frac{1}{2n_a} \begin{bmatrix} (n_a + n_s) e^{i\varphi_s} & (n_a - n_s) e^{-i\varphi_s} \\ (n_a - n_s) e^{i\varphi_s} & (n_a + n_s) e^{-i\varphi_s} \end{bmatrix}$$

$$\frac{1}{2n_s} \begin{bmatrix} (n_a + n_g) e^{i\varphi_g} & (n_s - n_g) e^{-i\varphi_g} \\ (n_s - n_g) e^{i\varphi_g} & (n_s + n_g) e^{-i\varphi_g} \end{bmatrix} \frac{1}{2n_g} \begin{bmatrix} (n_g + n_a) & (n_g - n_a) \\ (n_g - n_a) & (n_g + n_a) \end{bmatrix}$$

$\varphi_g = n_g k d_g$ where n_g and d_g are the refractive index and thickness of the glass substrate respectively. The other phase terms have the same meaning as in Eq. B.1. Upon simplifying, the transmission function is

$$t_{sppgs}(\phi) = \frac{t_0 t_{ag} t_{gs} t_{sa} e^{+in_g k d_g} e^{+i\alpha\phi}}{1 + r_{sa} r_{gs} e^{+i\beta(\phi+\phi_0)} + (r_{sa} e^{+i\beta(\phi+\phi_0)} + r_{gs}) e^{+2in_g k d_g} r_{ag}} \qquad (B.4)$$

The Fresnel transmission coefficients are $t_{ag} = \frac{2n_a}{n_g+n_a}$ (from air to glass), $t_{gs} = \frac{2n_g}{n_s+n_g}$ (glass to SPP etalon), $t_{sa} = \frac{2n_s}{n_s+n_a}$ (from SPP etalon to air), and the Fresnel reflection coefficients are $r_{ag} = \frac{n_a-n_g}{n_a+n_g}$ (from air to glass), $r_{gs} = \frac{n_g-n_s}{n_g+n_s}$ (glass to SPP etalon), and $r_{sa} = \frac{n_s-n_a}{n_s+n_a}$ (SPP etalon to air). $t_0 = e^{+in_a k \Delta h} e^{+in_s k h_0}$ is the same as in Chapter II. d_g and n_g is the thickness and refractive index of the glass substrate, respectively.

In chapters IV and V, the experimental transmittance of the spiral phase plate is fit to the modulus square of Eq. B.3:

$$T(\phi) = |t_{spp}(\phi)|^2 = \frac{A}{1 + \frac{4|r_2|^2}{(1-|r_2^{Fit}|^2)^2} \sin^2\left(\frac{\beta(\phi+\phi_0)}{2}\right)}, \qquad (B.5)$$

This equation does not include the role which the glass substrate of a different refractive index plays in determining the fit parameters of the optical angular interference pattern. In order to understand the role which the glass substrate plays in determining the fit parameters of chapters IV and V, in this section, data is generated using the transmission function with the glass substrate of different refractive index present, i.e. $|t_{sppgs}(\phi)|^2$ (modulus square of Eq. B.4), and fit to Eq B.5. This is done over a frequency window of about 35GHz as in chapter V. A spiral phase plate etalon with $d_g = 6.00mm$ (64), $k = \frac{2\pi}{632.991nm}$, $h_0 \approx 40\mu m$ (64), $\Delta h = 0.929\mu m$, $n_g = 1.470$ and $n_s = 1.56$ will have $\beta = 2n_s \frac{\Delta h}{\lambda} = 5.218$, $r_{sa} = 0.219$, $r_{gs} = -0.0303$, and $r_{ag} = -0.1901$. A plot of the transmission function at a single frequency with and without a glass substrate can be seen in Fig. B.1, and a plot of the various fit param-

101

Black line: Phase plate on glass substrate with different refractive index
Blue dashed line: Phase plate on glass substrate with same refractive index
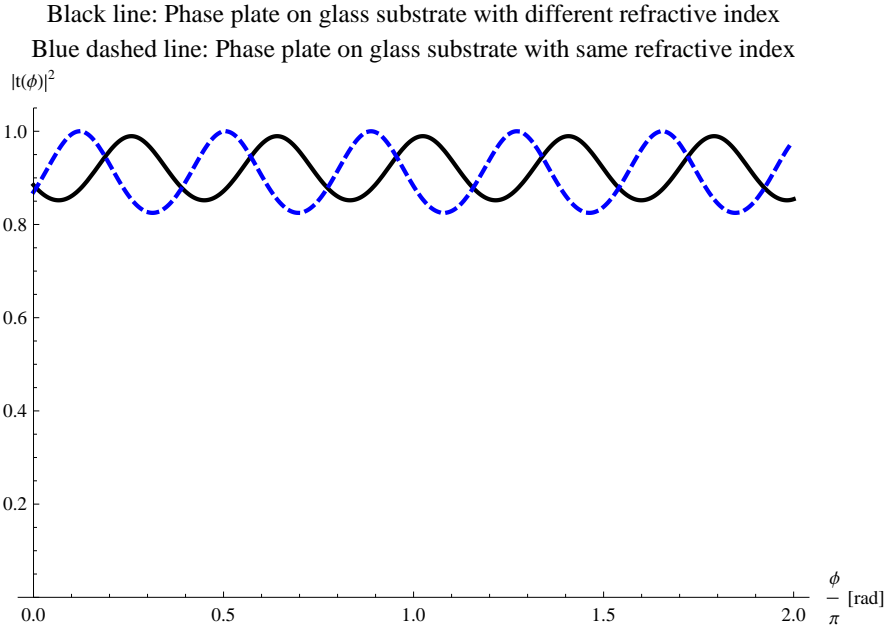
Figure B.1: Numerically calculated spiral phase plate etalon transmission function from transfer matrix with a glass substrate of the same (different) refractive index as SPP etalon which gives rise to a reflectivity of 0.219 (0.192) and a modulation amplitude of 0.175 (0.161) when $\beta = 5.218$ at a laser frequency of 539.372380THz. As the laser frequency is varied in the thin plate approximation, the modulation frequency stay constant, but there is a change in the modulation amplitude when the glass substrate sits on a glass substrate with different refractive index. The fit parameters as they depend on frequency is in fig. B.2.
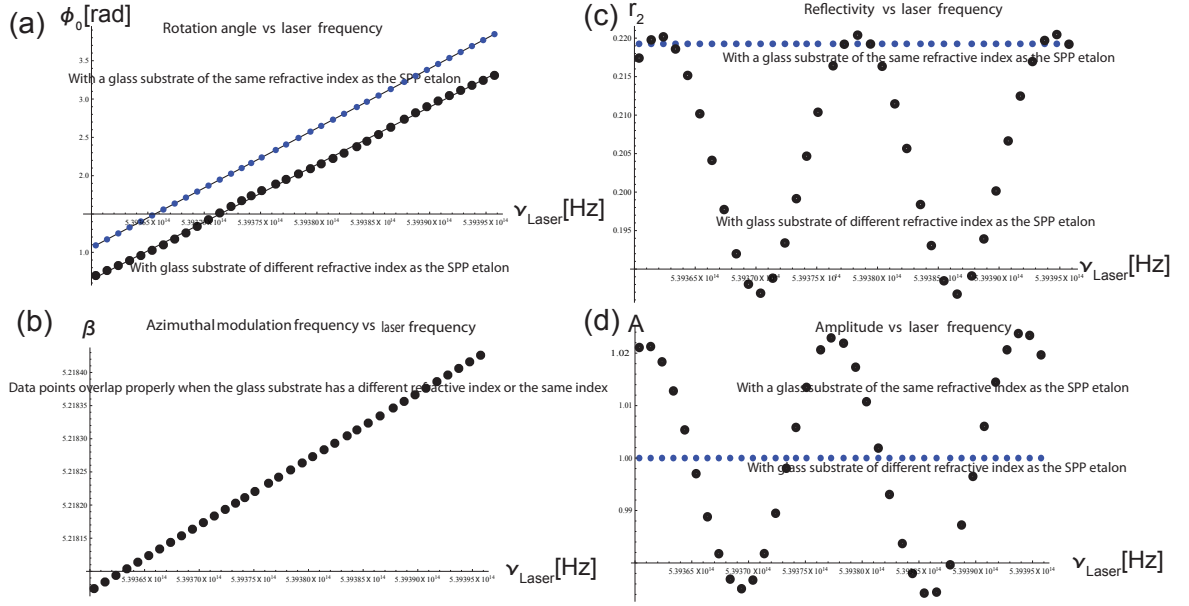
Figure B.2: Parameters of the spiral phase plate etalon when the calculated transmission function with a glass substrate of the same refractive index as the SPP etalon (Blue dots), $|t_{spp}|^2$, is fit to the transmission function with the glass substrate of a different refractive index as the SPP etalon (Black circles), $|t_{sppgs}|^2$, when the laser frequency is varied from 539.360380THz to 539.395750THz for (a) position of interference pattern, ϕ_0, (b) angular modulation frequency, β, (c) reflectivity, r_2, and (d) peak of the angular interference pattern, A. The modulation frequency, β, is not affected by the difference in refractive index of the SPP etalon and glass substrate. In addition, the position parameter does not appear to be affected significantly by the presence of the glass substrate, i.e. the slope of the ϕ_0 fit parameter for the two cases agree to within 0.18 standard deviations in units of the fit error, $\frac{d\phi_0}{d\nu_{Laser}} = (8 \pm 2) \times 10^{-11}$. However, the other parameters are affected by the presence of a glass substrate with different refractive index from the SPP etalon. The reflectivity parameter, r_2, displays a periodic oscillatory curve shown in (c). When a glass substrate of different refractive index is present, the reflectivity parameter, r_2, has an upper limit in the neighborhood of the reflectivity parameter when the SPP etalon and glass substrate has the same refractive index. This result agrees qualitatively with the experimental data in Chapter V. The amplitude parameter has a similarly shaped curve as the reflectivity parameter, but the upper limit can have a value larger than the case when the SPP etalon and glass substrate have the same refractive index.

eters (ϕ_0, β, r_2, A) as a function of laser frequency over a 35GHz range, (539.360380 THz to 539.395750THz THz), with increments of approximately 1GHz.

While the glass substrate of different refractive index introduces a constant phase shift to the phase of the transmission function describing the angular interference pattern and reduces the modulation amplitude, $A_{mod} = \frac{4r_2^2}{(1+r_2^2)^2}$, compared to the case of a device with a glass substrate of the same refractive index as the SPP etalon, it does not change the modulation frequency, β. An example to illustrate this effect is in Fig. B.1 and B.2. As the laser frequency is changed, the value of the modulation frequency is the same for both cases. The value of β changes at the level of $\delta\beta \approx \beta\frac{\delta\nu}{\nu} \approx 10^{-4}$ over a 35GHz range. This value is much smaller than the shot noise limited error bar of chapters IV and V. The position parameter, ϕ_0 has comparable slopes for the case of an SPP etalon on a glass substrate with same refractive index as the glass substrate, and for the case of an SPP etalon of a glass substrate with different refractive index. The agreement is at the level of 0.18 standard deviations, where the slope is $\frac{d\phi_0}{d\nu_{Laser}} = (8 \pm 2) \times 10^{-11}$. It must be noted that it is the absolute value of the slope that is used to make a comparison between the experiment and theory. When the theory is compared to the experiment in chapter V, the experiment is found to be consistent at the 3% level (2 std. dev) for experimental measurements taken in the increasing frequency direction.

The parameter quantifying the reflectivity and peak amplitude parameters displays a periodic oscillation as a function of laser frequency in Fig. B.2(c). The upper limit of the reflectivity parameter is in the neighborhood for the case were the refractive index of the glass substrate and SPP etalon are the same. The shape of this curve is apparent in the experimental data presented in chapter V, which is in qualitative agreement with the theory presented in this section. The calculated peak amplitude parameter, A, displays a similar shaped curve for the reflectivity parameter. Nevertheless, in the analysis of the experimental data, the peak of the angular

interference pattern tends to be overwhelmed by the relative intensity fluctuation between the vortex laser beam normalized with the Gaussian laser beam and it is generally normalized to 1 or a value close to 1, and therefore a direct comparison between experiment and Fig B.2(d) cannot be made.

In a way, the parameters obtained from fitting the experimental data to Eq. B.5 can be considered fictitious in nature since the fitting model does not explicitly take into account physical effects arising from the glass substrate of a different refractive index. Note that it is more appropriate to use these fictitious parameters to check for agreement or disagreement between experiment and theory since the experimental data is fit to Eq. B.5, $|t_{spp}|^2$, and not the modulus square of Eq. B.4, $|t_{sppgs}|^2$.

APPENDIX C

CCD noise and error bar estimation due to photo-detection

This appendix discuss the time average and ensemble average of photo-counts arriving at the CCD detector, and discuss the origins of the error bar on the data. The first paragraph of the section on "Computer generated optical intensity" in section 3.5 of chapter III describes the time average of photo-counts when the CCD integration time is long compared to the characteristic time scale of the fluctuations in the intensity and phase. Hence the noise in the field's intensity is averaged out. When an ensemble of all the vortex counts normalized with Gaussian pixel counts (described by Eq. 3.13 in Chapter III) on the CCD array is plotted as a function of angle (i.e. Fig. 3.6 (a)), the noise in the field's intensity and detector shows up as a broadening in the histogram's width (e.g. Fig. 3.6(c)) for an angular wedge of the transmission function. This is because the counts in each pixel in the Gaussian shaped laser beam fluctuates about the mean described by Eq. C.1, or in the case of data limited by shot-noise, it fluctuates by $\sqrt{N} = \sqrt{\eta \langle I \rangle \tau_{ccd}}$; where N is the number of counts in each pixel, η is related to the efficiency of the detector, $\langle I \rangle$ is the average intensity, and τ_{CCD} is the integration time of the CCD. An upper limit on the width of the histogram for an angular wedge (single bin) of the transmission function is shown in

Fig. 3.6 (c), will scale as $\frac{N_V + \sqrt{N_V}}{N_G - \sqrt{N_G}} - \frac{N_V - \sqrt{N_V}}{N_G + \sqrt{N_G}} \propto \frac{1}{\sqrt{N}}$. It has been assumed that the number of counts in the vortex pixels and Gaussian pixels are approximately equal, and the number of counts in each pixel is $N \gg 1$. These fluctuations in the noise can be averaged out by dividing the optical intensity profiles into angular wedges, and taking a weighted ensemble average of the data points in each wedge to represent one binned data point (e.g. Fig. 3.6 (b)). The noise will show up in the error bar estimation of each bin. The fluctuation in number counts from a single pixel is (70; 71):

$$\Delta m^2 \left(\tau_{ccd} \right) = \eta \left\langle I \right\rangle \tau_{ccd} + \eta^2 \tau_{ccd}^2 \left[\left\langle I^2 \right\rangle - \left\langle I \right\rangle^2 \right] \tag{C.1}$$

where the contribution from shot noise is $\eta \left\langle I \right\rangle \tau_{ccd}$ and the field intensity fluctuation is $\eta^2 \tau_{ccd}^2 \left[\left\langle I^2 \right\rangle - \left\langle I \right\rangle^2 \right]$. η is related to the detector efficiency, τ_{ccd} is the CCD integration time, and I is the intensity. In the computer generated data, it has been assumed that there is no fluctuation in the intensity of the laser beam, therefore the second term in Eq. C.1 is zero. It is for this reason that it is called "shot-noise limited computer generated data" or "shot-noise limited simulations". In quantifying the experimental data, it is the relative fluctuations between the vortex and Gaussian beam that is of consequence since a pixel by pixel normalization of the vortex laser beam with the Gaussian laser beam is performed. This fluctuation will show up in the fit parameter error bars as seen in the experimental fit parameter histograms of chapter IV. In the event that there are large fluctuations ($> \frac{1}{2}$ the peak intensity) in the relative intensity between the vortex and Gaussian beam, the $\frac{1}{e^2}$ beam radius will change from shot to shot, and the histograms of the individual fit parameters is expected to be much broader and could even deviate from resembling a normal distribution. Distortions in the optical intensity profile could also result in the histograms deviating from a normal distribution. Both of these items have been observed when analyzing some of the experimental data.

Bibliography

[1] C. Fabry and A. Perot, Sur les franges des lames minces argente es et leur application a' la mesure de petites epaisseurs dair, Ann. Chim. Phys. 12, 459501 (1897)

[2] R. A. Beth, Direct detection of the angular momentum of light, Phys. Rev. **48**, 471 (1935).

[3] R. A. Beth, Mechanical detection and measurement of the angular momentum of light, Phys. Rev. **50**, 115 (1936).

[4] L. Allen, M.J. Padgett, and M. Babiker, The orbital angular momentum of light, Prog. in Optics XXXIX, 291 (1999)

[5] L. Allen, M. W. Beijersbergen, R. J. C. Spreeuw, and J. P. Woerdman, Orbital angular momentum of light and the transformation of Laguerre-Gaussian modes, Phys. Rev. A **45**, 8185 (1992).

[6] S. M. Barnett and L. Allen, Orbital angular momentum and nonparaxial light beams, Opt. Commun. **110**, 670 (1994).

[7] S. M. Barnett, Optical angular-momentum flux, J. Opt. B **4**, S7 (2002).

[8] A. Mair, A. Vaziri, G. Weihs, and A. Zeilinger, Entanglement of the orbital angular momentum states of photons, Nature **412**, 313 (2001).

[9] G. Gibson, J. Courtial, M. Padgett, M. Vasnetsov, V. Pas'ko, S. Barnett, and S. Franke-Arnold, Free-space information transfer using light beams carrying orbital angular momentum, Opt. Express **12**, 5448 (2004).

[10] S. S. R. Oemrawsingh, A. Aiello, E. R. Eliel, G. Nienhuis, and J. P. Woerdman, How to observe high-dimensional two-photon entanglement with only two detectors, Phys. Rev. Lett. **92**, 217901 (2004).

[11] A. Aiello, S. S. R. Oemrawsingh, E. R. Eliel, and J. P. Woerdman, Nonlocality of high-dimensional two-photon orbital angular momentum states, Phys. Rev. A **72**, 052114 (2005).

[12] S. S. R. Oemrawsingh, X. Ma, D. Voigt, A. Aiello, E. R. Eliel, G. W. 't Hooft, and J. P. Woerdman, Experimental demonstration of fractional orbital angular momentum entanglement of Two Photons, Phys. Rev. Lett. **95**, 240501 (2005).

[13] Z. Dutton and J. Ruostekoski, Transfer and storage of vortex states in light and matter waves, Phys. Rev. Lett. **93**, 193602 (2004).

[14] K. T. Kapale and J. P. Dowling, Vortex phase qubit: Generating arbitrary, counter-rotating, coherent superpositions in Bose-Einstein condensates via optical angular momentum beams, Phys. Rev. Lett. **95**, 173601 (2005).

[15] S. Thanvanthri, K. T. Kapale, and J. P. Dowling, Arbitrary coherent super-positions of quantized vortices in Bose-Einstein condensates via orbital angular momentum of light, Phys. Rev. A **77**, 053825 (2008).

[16] B. Jack, P. Aursand, S. Franke-Arnold, D.G. Ireland, J. Leach, S.M. Barnett, and M. J. Padgett, Demonstration of the angular uncertainty principle for single photons, J. Opt. **13**, 064017 (2011).

[17] S. Franke-Arnold, S.M. Barnett, E. Yao, J. Leach, J. Courtial and M. J. Padgett, Uncertainty principle for angular position and angular momentum, New J. Phys. **6**, 103 (2004).

[18] M.P.J. Lavery, A. Dudley, A. Forbes, J. Courtial and M.J. Padgett, Robust interferometer for the routing of light beams carrying orbital angular momentum, New J. Phys., **13** 093014 (2011)

[19] J. Leach, J. Courtial, K. Skeldon, S.M. Barnett, S. Franke-Arnold and M.J. Padgett, Interferometric methods to measure orbital and spin, or the total angular momentum of a single photon, Phys. Rev. Lett. **92** 013601 (2004)

[20] J. Leach, M. J. Padgett, S.M. Barnett, S. Franke-Arnold, J. Courtial, Measuring the orbital angular momentum of a single photon, Phys. Rev. Lett. **88** 257901 (2002)

[21] M. Harris, C. A. Hill, P.R. Tapstar, and J.M. Vaughan, Phys. Rev. A. **49**, 3119 (1994).

[22] J. Vickers, M. Burch, R. Vyas, S. Singh, Phase and interference properties of optical vortices, J. Opt. Soc. Am. A **25**, 823 (2008).

[23] M. Padgett, J. Arlt, N. Simpson, and L. Allen, An experiment to observe the intensity and phase structure of Laguerre-Gaussian laser modes, Am. J. Phys. **64**, 77-82 (1996).

[24] M. F. Andersen, C. Ryu, P. Cladé, V. Natarajan, A. Vaziri, K. Helmerson, and W. D. Phillips, Quantized rotation of atoms from photons with orbital angular momentum, Phys. Rev. Lett. **97**, 170406 (2006).

[25] C. Ryu, M. F. Andersen, P. Clad, V. Natarajan, K. Helmerson and W. D. Phillips, Observation of Persistent Flow of a Bose-Einstein Condensate in a Toroidal Trap, Phys. Rev. Lett. **99**, 260401 (2007).

[26] A. Ramanathan, K. C. Wright, S. R. Muniz, M. Zelan, W. T. Hill, III, C. J. Lobb, K. Helmerson, W. D. Phillips, and G. K. Campbell, Superflow in a Toroidal Bose-Einstein Condensate: An Atom Circuit with a Tunable Weak Link, Phys. Rev. Lett. **106**, 130401 (2011).

[27] R. Kanamoto, E. M. Wright, and P. Meystre, Quantum dynamics of Raman-coupled Bose-Einstein condensates using Laguerre-Gaussian beams, Phys. Rev. A **75**, 063623 (2007).

[28] S. Franke-Arnold, J. Leach, M. J. Padgett, V. E. Lembessis, D. Ellinas, A. J. Wright, J. M. Girkin, P. Ohberg, and A. S. Arnold, Optical ferris wheel for ultracold atoms, Opt. Express **15**, 8619 (2007).

[29] T. P. Simula, N. Nygaard, S. X. Hu, L. A. Collins, B. I. Schneider, and K. Mølmer, Angular momentum exchange between coherent light and matter fields, Phys. Rev. A **77**, 015401 (2008).

[30] K. C. Wright, L. S. Leslie, and N. P. Bigelow, Optical control of the internal and external angular momentum of a Bose-Einstein condensate, Phys. Rev. A **77**, 041601 (2008).

[31] K. C. Wright, L. S. Leslie, A. Hansen, and N. P. Bigelow, Sculpting the vortex state of a spinor BEC, Phys. Rev. Lett. **102**, 030405 (2009).

[32] D. L. Andrews, ed., *Structured Light and Its Applications: An Introduction to Phase-Structured Beams and Nanoscale Optical Forces* (Elsevier, 2008).

[33] J. E. Curtis and D. G. Grier, Structure of optical vortices, Phys. Rev. Lett. **90**, 133901 (2003).

[34] D. G. Grier, A revolution in optical manipulation, Nature **424**, 810 (2003).

[35] V. Garces-Chavez, D. McGloin, M. J. Padgett, W. Dultz, H. Schmitzer and K. Dholakia, Observation of the transfer of the local angular momentum density of a multiringed light beam to an optically trapped partical, Phys. Rev. Lett. **91**, 133901 (2003)

[36] M. Padgett and R. Bowman, Tweezers with a twist, Nat. Photon **5**, 343 (2011).

[37] J. M. Vaughan and D. V. Willetts, Temporal and interference fringe analysis of TEM01 laser modes, J. Opt. Soc. Am. **73**, 1018 (1983).

[38] F. B. de Colstoun, G. Khitrova, A. V. Fedorov, T. R. Nelson, C. Lowry, T. M. Brennan, B. G. Hammons, and P. D. Maker, Transverse modes, vortices and vertical-cavity surface-emitting Lasers, Chaos, Solitons & Fractals **4**, 1575 (1994).

[39] V. Yu. Bazhenov, M. V. Vasnetsov, and M. S. Soskin, Laser beams with screw dislocations in their wavefronts, JETP Lett. **52**, 429 (1990).

[40] V. Yu. Bazhenov, M. S. Soskin, and M. V. Vasnetsov, Screw dislocations in light wavefronts, J. Mod. Opt. **39**, 985 (1992).

[41] N. R. Heckenberg, R. McDuff, C. P. Smith, H. Rubinsztein-Dunlop, and M. J. Wegener, Laser beams with phase singularities, Opt. Quantum Electron. **24**, S951 (1992).

[42] N. R. Heckenberg, R. McDuff, C. P. Smith, and A. G. White, Generation of optical phase singularities by computer-generated holograms, Opt. Lett. **17**, 221 (1992).

[43] S. van Enk and G. Nienhuis, Eigenfunction description of laser beams and orbital angular momentum of light, Opt. Commun. **94**, 147 (1992).

[44] M. W. Beijersbergen, L. Allen, H. E. L. O. van der Veen, and J. P. Woerdman, Astigmatic laser mode converters and transfer of orbital angular momentum, Opt. Commun. **96**, 123 (1993).

[45] M. J. Padgett and L. Allen, Orbital angular momentum exchange in cylindrical-lens mode converters, J. Opt. B **4**, S17 (2002).

[46] S. S. R. Oemrawsingh, J. A. W. van Houwelingen, E. R. Eliel, J. P. Woerdman,E. J. K. Verstegen, J. G. Kloosterboer, and G. W. 't Hooft, Production and characterization of spiral phase plates for optical wavelengths, Appl. Opt. **43**, 688 (2004).

[47] N. Yu, P. Genevet, M. A. Kats, F. Aieta, J-P Tetienne, F. Capasso, Z. Gaburro1, Light Propagation with phase discontinuities: Generalized laws of reflection and refraction, Science, **334** 333 (2011)

[48] M. W. Beijersbergen, R. P. C. Coerwinkel, M. Kristensen, and J. P. Woerdman, Helical-wavefront laser beams produced with a spiral phase plate, Opt. Commun. **112**, 321 (1994).

[49] M. V. Berry, Optical vortices evolving from helicoidal integer and fractional phase steps, J. Opt. A **6**, 259 (2004).

[50] J. B. Götte, S. Franke-Arnold, R. Zambrini, and S. M. Barnett, Quantum formulation of fractional orbital angular momentum, J. Mod. Opt. **54**, 1723 (2007).

[51] J. B. Götte, K. O'Holleran, D. Preece, F. Flossmann, S. Franke-Arnold, S. M. Barnett, and M. J. Padgett, Light beams with fractional orbital angular momentum and their vortex structure, Opt. Express **16**, 993 (2008).

[52] J. B. Götte, J Leach, E. Yao, M. Padjett, Observation of the vortex structure of non-integer vortex beam, New J. Phys. **6**, 71 (2004).

[53] G. Milione, S. Evans, D. A. Nolan, R. R. Alfano, Higher order Pancharatnam-Berry phase and the angular momentum of light, Phys. Rev. Lett. **108**, 190401 (2012).

[54] G. Molina-Terriza, J. P. Torres, and L. Torner, Twisted photons, Nat. Phys. **3**, 305 (2007).

[55] S. Franke-Arnold and M. Padgett, Advances in optical angular momentum, Laser & Photon. Rev. **2**, 299 (2008).

[56] A. V. Carpentier, H. Michinel, J. R. Salgueiro, and D. Olivieri, Making optical vortices with computer-generated holograms, Am. J. Phys. **76**, 10 (2008)

[57] A. E. Siegman, *Lasers* (University Science Books, 1986).

[58] M. Born and E. Wolf, *Principles of Optics* (Cambridge University Press, 1999), 7th ed.

[59] J. W. Goodman, *Introduction to Fourier Optics* (Roberts & Company Publishers, 2005), 3rd ed.

[60] B. E. A. Saleh and M. C. Tiech, *Fundamentals of photonics* (Wiley-interscience, 2007), 2nd ed.

[61] K. Kinosita, Numerical evaluation of the intensity curve of a multiple-beam fizeau fringe, J. Phys. Soc. Japn. **8**, 2 (1953)

[62] M. A. Rob, Limitation of a wedge etalon for high-resolution linewidth measurements, Opt. Lett. **15**, 11 (1990)

[63] T. T. Kajava, H. M. Lauranto, R. R. E. Solomaa, Fizeau interferometer in spectral measurements, J. Opt. Soc. Am. **10**, 11 (1993)

[64] RPC Phontonics, http://www.rpcphotonics.com/.

[65] J.P. Torres, and L. Torner. Twisted Photons: Applications of Light with Orbital Angular Momentum, (Bristol: Wiley-VCH, 2011)

[66] L. Allen, S.M. Barnnet, and M.J. Padgett Optical Angular Momentum, (Bristol: Institute of Physics, 2003).

[67] S. Franke-Arnold, S. M. Barnett, E. Yao, J. Leach, J. Courtial, and M. Padgett, Uncertainty principle for angular position and angular momentum, New J. Phys. **6**, 103 (2004).

[68] E. Yao, S. Franke-Arnold, J. Courtial, S. Barnett, and M. Padgett, Fourier relationship between angular position and optical orbital angular momentum, Opt. Express **14**, 9071 (2006).

[69] B. Jack, M. J. Padgett, and S. Franke-Arnold, Angular diffraction, New J. Phys. **10**, 103013 (2008).

[70] P. R. Berman and V. S. Malinovsky, Principles of laser spectroscopy and quantum optics, 339-343 (Princeton University press, 2011)

[71] R. Loudon, The quantum theory of light, (Oxford University press, 2000)

[72] See Appendix C

[73] P. R. Bevington and D. K. Robinson, Data reduction and error analysis for the physical sciences, (McGraw-Hill, 1992)

[74] J. R. Taylor, An introduction to error analysis; The study of uncertainties in physical measurements, (Oxford University press, 1982)

[75] R. A. Maronna, D. R. Martin and V. J. Yohai, Robust statistics; Theory and methods 31-32 (Wiley, 2006)

[76] B. Efron, R. Tibshirani, Bootstrap methods for standard errors, confidence intervals and other measures of statistical accuracy. Stat. Sci. **1**, 54-75 (1986)

[77] B. Efron, Better bootstrap confidence intervals. J. Am. Stat. Assoc. **82**, 1, 171-185 (1987)

[78] J. J. Hudson, D. M. Kara, I. J. Smallman, B. E. Sauer, M. R. Tarbutt, E. A. Hinds, Improved measurement of the shape of the electron. Nature **473**, 493-497 (2011)

[79] http://www.princetoninstruments.com/

[80] http://www.thorlabs.com/

[81] M. Dobusz and M. Kozuchowski, Frequency stabilization of a diode by means of an optical angular wedge, Meas. Sci. Technol **23**, 1-9 (2012).

[82] T. Carmon, L. Yang, K.J. Vahala, Dynamical thermal behavior and thermal self stability of microcavities, Opt. Express **12**, 4742 (2004).

[83] V. S. Ilchenko and M. L. Gorodetskii, Thermal nonlinear effects in optical whispering gallery microresonators, Laser Phys. **2**, 1004 (1992)

[84] M. L. Gorodetsky, and I. S. Grudinin, Fundamental thermal fluctuations in microspheres, J. Opt. Soc. Am. B **21**, 697, (2004).

[85] T. Carmon, T. J. Kippenberg, L. Yang, H. Rokhsari, S. Spillane, and K. J. Vahala, Feedback control of ultra-high-Q microcavities: application to micro-Raman lasers and micro parametric oscillators, Opt. Express **13**, 3558 (2005)